INDONESIAN JOURNAL ON GEOSCIENCE
Geological Agency
Ministry of Energy and Mineral Resources

Journal homepage: http://ijog.geologi.esdm.go.id
ISSN 2355-9314, e-ISSN 2355-9306

# Magmatic Evolution and Plumbing System of Gede-Salak Volcano, Banten, Indonesia

[1,2]Muhammad Alfath Salvano Salni, [1]Euis Tintin Yuningsih, and [2]Tsukasa Ohba

[1]Faculty of Geological Engineering, Universitas Padjadjaran, Jatinangor 45363, Indonesia
[2]Graduate School of International Resource Sciences, Akita University, Akita 010-8502, Japan

Corresponding author: alfath.salvano@gmail.com
Manuscript received: October, 06, 2022; revised: January, 13, 2023;
approved: May, 14, 2023; available online: August, 10, 2023

**Abstract** – The study of individual volcanoes in northwest Java has been largely overlooked. In this study, an investigation of the magma evolution and plumbing system of Gede-Salak Volcano was conducted. A geological survey determined the lava unit and volcanism. The whole-rock geochemistry is utilized to determine the magma type and evolution. Mineral chemistry based on microprobe analysis revealed the magmatic process and phenocryst origin. Geothermobarometry is employed to estimate the temperature and pressure. The volcanism comprised the eruption of lava flows, sector collapse, and the eruption of lava domes. The magma evolution consists of two magma types: type A (lava flow and peripheral dome) and type B (summit dome). The processes identified are amphibole fractionation, magma mixing, and crust assimilation. Phenocryst textures and chemistry implied open-system processes in the plumbing system involving three magma series, namely the felsic, intermediate, and mafic series. Magma type A resulted from multiple mafic recharges on the felsic series, while type B resulted from the mixing of intermediate and mafic series. The felsic and intermediate phenocryst crystallization occurred at 933-948°C and 1010-1011°C in the mid-crust at 14 km to 17 km depth. Meanwhile, the mafic series reside in the lower crust at 21 km depth and of 1065-1087°C temperature.

**Keywords**: Gede-Salak, magma evolution, magma plumbing, geothermobarometry, mineral chemistry

© IJOG - 2023

**How to cite this article:**
Salni, M.A.S., Yuningsih, E.T., and Ohba, T., 2023. Magmatic Evolution and Plumbing System of Gede-Salak Volcano, Banten, Indonesia. *Indonesian Journal on Geoscience*, 10 (2), p.245-276. DOI: 10.17014/ijog.10.2.245-276

## Introduction

### Background

The magma plumbing system is an essential puzzle in understanding the volcano behaviour. The magma plumbing system comprises the network of magma production, storage, transport channels, and chambers underlying volcanic regions (Burchardt, 2018). To comprehend the magma plumbing system, a number of magma characteristics must be investigated. Among these characteristics are magmatic processes during evolution, magma emplacement depths, magma chamber composition, and early-formed crystal nature (Hasibuan, 2020). Therefore, a comprehensive data set comprising lava stratigraphy, whole-rock geochemistry, and mineral chemistry is compulsory to establish a magma plumbing system.

Magma evolution and plumbing system in calc-alkaline volcanic rocks have been attributed to periodic influxes of deep mafic magma to shallow felsic magmas, *e.g.* Krakatau (Dahren *et al.*,

2012), Rajabasa (Hasibuan, 2020), and Sindoro, For instance, Rajabasa Volcano resulted from the interaction of a single felsic end-member magma with three mafic end-member magmas. The storage region varied from evolved magma in the upper crust to hot primitive magma in the mantle interface (Hasibuan, 2020).

The magma and its plumbing evolution of Sunda Arc volcanoes have been the subject of numerous studies. However, northwest Java volcanoes have been largely overlooked. Previous studies have been conducted to compare the geochemical variation of the northwest Java volcanoes to other volcanoes on Java Island (Kurniawan *et al*., 2011, 2013). However, the individual magmatic evolution of a volcano has not yet been studied. This study investigates the magmatic evolution and plumbing system of a volcano in northwest Java, namely the Gede-Salak Volcano.

**Geotectonic Setting of Sunda Arc**

Gede-Salak Volcano is situated within Sunda volcanic arc. Sunda arc develope from the subduction of Indo-Australian Plate beneath Eurasian Plate at a rate of 6-7 cm/year (Hamilton, 1973; Widiyantoro and van der Hilst, 1997). The arc covers a distance of about 3,200 km, from Sumatra in the west to Flores in the east. The overriding crust of Sunda arc is characteristically shifted from continental type to oceanic crust toward the east. The subducting plate can also exhibit variability along the arc. The age of the subducting Indian Ocean Crust differs in West Java (~80 Ma) and East Java (~130 Ma) (Hamilton, 1973). The composition and mass of sediments in Java Trench also vary along the island (Handley *et al.*, 2014). Hall (2012) discussed the complete tectonic context of the subduction in the Indonesian region.

Gede-Salak Volcano is positioned adjacent to Sunda Strait. The Sunda Strait is a unique volcanic region in Sunda Arc that serves as a transitional zone between Java perpendicular and Sumatra oblique subductions (Huchon and Le Pichon, 1984). Aside from the subduction-associated compression, the strait undertook extension due to the clockwise rotation of Sumatra relative to Java since Late Cenozoic (Harjono *et al*., 1991). The rotational movement is associated with a shift in the convergence angle from nearly orthogonal (12°) in front of Java to oblique (57°) in front of Sumatra. The geodynamic complexity has produced one of Indonesia most active tectonic and volcanic zones (Huchon and Le Pichon, 1984).

**Geology of Gede-Salak Volcano**

Gede-Salak Volcano is administratively located in the Banten Province, on the northwestern tip of Java Island. The name is derived from two highest peaks in the area. The volcano has a dimension of about 12 km x 12 km. Gede-Salak Volcano is reckoned as a rear-arc volcano within the northwest Java lineament with a slab depth of around 150 km (Hayes *et al.*, 2018). The distance from Java Trench is about 300 km. Rawa Danau Caldera is situated to the south within the volcanic lineament.

Regional geological map of Serang Quadrangle, Indonesia, portrays Gede-Salak as a Pleistocene volcanic product (Rusmana *et al.*, 1991). Kurniawan *et al.* (2013) proposed that the volcanism of Gede-Salak Volcano is divided into two stages: precaldera and postcaldera. The precaldera stage comprised pyroclastic flow deposits in the west and lava flows in the east. The dome formation at the centre and the southeast parts characterizes postcaldera activity. Gede-Salak is overlapped by Plio-Quaternary Tuffs (Banten Tuff) ranging in age from 0.07 to 0.1 Ma (Pramumijoyo and Sebrier, 1991).

The geological structure seems to influence the development of the volcano. Various geophysical methods, including gravity gradient (Suntoko and Nugroho, 2011), magnetic (Suntoko *et al.*, 2012), and seismic refraction (Suntoko and Mellawati, 2014) have been used to investigate the subsurface structure of the Gede-Salak Volcano and its surroundings. These studies revealed the presence of four faults. The kinematic study of subsidiary structure estimates the relative movement and stress orientation. The structures are

classified as sinistral faults formed by the main compression tectonic force, west-east trending. Faults in the southeast flank form a transtension zone that could provide a pathway for magma that erupts as lava domes in a corresponding NW - SE trend (Widagdo *et al.*, 2021).

## Methods and materials

### Methods

A geological mapping of Gede-Salak Volcano was conducted through morphological analyses and field observation. Advanced Spaceborne Thermal Emission and Reflection Radiometer Global Digital Elevation Model (ASTER GDEM) was used to delineate each lava unit utilizing ArcGIS Pro. NASA Earth Data provides open access to ASTER GDEM data. Field observation was conducted to ascertain the delineated unit from morphological analyses and sample collection. The study collected thirty-four fresh lava samples from Gede-Salak Volcano. Three lava flow units, two summit domes, and a group of small lava dome units were included in the sampling. Thin sections and rock powders were prepared from each sample for petrography, mineral chemistry, and whole-rock chemical analyses. Petrographic observations were conducted at Akita University using a Nikon Eclipse E600 POL microscope.

Major and selected trace element compositions of whole-rock were determined by X-ray fluorescence analyses (XRF) utilizing ZSX Primus II installed at Akita University. The samples were prepared using the glass bead method. The compositions were determined by matrix-corrected calibration curves obtained from the measurements of fifteen Geological Survey of Japan (GSJ) igneous series samples. Additional trace element compositions, including Rare Earth Elements (REE), were determined by inductively coupled plasma mass spectrometry (ICP-MS) employing Agilent 8900 ICP-MS Triple Quad installed at Akita University. The samples were prepared using a wet digestion method.

Backscattered electron (BSE) images and microprobe analyses were performed in several sessions using Electron Micro Probe Analyzer (EPMA) utilizing JEOL JXA 8800 installed at Akita University. The EPMA analyses is used to examined the phenocrysts of plagioclase, pyroxene, and amphibole. The conditions for the quantitative analyses were set at 15 kV for accelerating voltage, 20 nA for beam current, 2-15 µm for probe diameter, 10-20 s for peak counting times, and oxide and ZAF for correction method. Synthetic minerals that were used as standards are jadeite for Si and Na, rutile for Ti, corundum for Al, chromium oxide for Cr, hematite for Fe, manganosite for Mn, periclase for Mg, wollastonite for Ca, and $KTiPO_4$ for K. Element condition of measurement was ordered in: Channel 1 (TAP crystal) for Si and Al; Channel 2 (PETJ crystal) for K, Ca, and Ti; Channel 3 (LIF crystal) for Fe, Cr, and Mn; and Channel 4 (TAP crystal) for Na and Mg. Na was analyzed in the first sequence to minimize Na loss during analyses.

Geothermobarometry was employed to estimate the temperature and pressure conditions of phenocryst crystallization. The model was chosen based on the appropriate pairs of mineral and/or melt composition equilibrium. The equilibrium was tested by comparing the exchange coefficients of elements. The models employed in this study are amphibole-plagioclase (Holland and Blundy, 1994); clinopyroxene-melt (Putirka, 2008 Neave and Putirka, 2017), two pyroxenes (Putirka, 2008), and amphibole-only (Ridolfi, 2021).

The depth calculation was obtained by converting geobarometric pressure to depth using densities and thicknesses of the respective stratigraphic units beneath the volcano. The density value of crustal lithologic units was acquired based on the seismic study on Sunda Strait (Kopp *et al.*, 2001). The accumulated depth of the lithologic unit was obtained from an analyses of teleseismic receiver functions located close to Gede-Salak Volcano (~10 km) (Anggono *et al.*, 2020). summary of the parameter used in depth calculation is shown in Table 1.

Table 1. Estimated Density Values and Depth of Crustal Rocks Beneath Gede-Salak

| Inferred rock types | Depth (km) (Anggono *et al.*, 2020) | Average density (g/cm$^3$) (Kopp *et al.*, 2001) |
|---|---|---|
| Sedimentary layers | 0-2 | 2.50 |
| Granitoids | 2-10 | 2.89 |
| Diorite or gabbro | 10-28 | 2.95 |
| Mantle | >28 | 3.37 |

## Result and analyses

### Volcanism of Gede-Salak Volcano

Gede-Salak Volcano has lost some of its original morphology due to advanced stages of erosion. However, the general morphology of the lava flow and dome are mostly preserved to be delineated. Volcanism of Gede-Salak was summarized as follows: eruption of andesitic lava flows, formation of sector collapse, and the development of the summit dome at the centre and peripheral dome on the southeast flank. Geological map and stratigraphy are depicted in Figure 1.

Its volcanism commenced with the eruption of andesitic lava flow consisting of Batu lava flow (Blv), Salak lava flow (Slv), and Gede lava flow (Glv). The lava flows exhibit typical characteristic of subaerial andesitic lava. The deposit developed a massive structure (Figure 2a) with occasional prismatic joints. Lava flows occasionally display well-developed sheeted joints (Figure 2b).

The subsequent volcanism formed ~8 km$^2$ circular depression at the southeast flank, previously attributed to caldera formation (Kurniawan *et al.*, 2013). However, a caldera is typically identified by an extensive peripheral outflow sheet containing a caldera-forming eruption sequence which is absent in the volcano. The feature is probably the result of sector collapse. It exhibits an open-sided amphitheater with a horseshoe-shaped valley, likely caused by outward-directed sector collapse landslide down flanks of unstable volcanoes (de Silva and Lindsay, 2015). The sector collapse deposited the Batur debris avalanche (Bda) on the southeast flank. The deposit is characteristically nongraded and poorly sorted, with andesite and

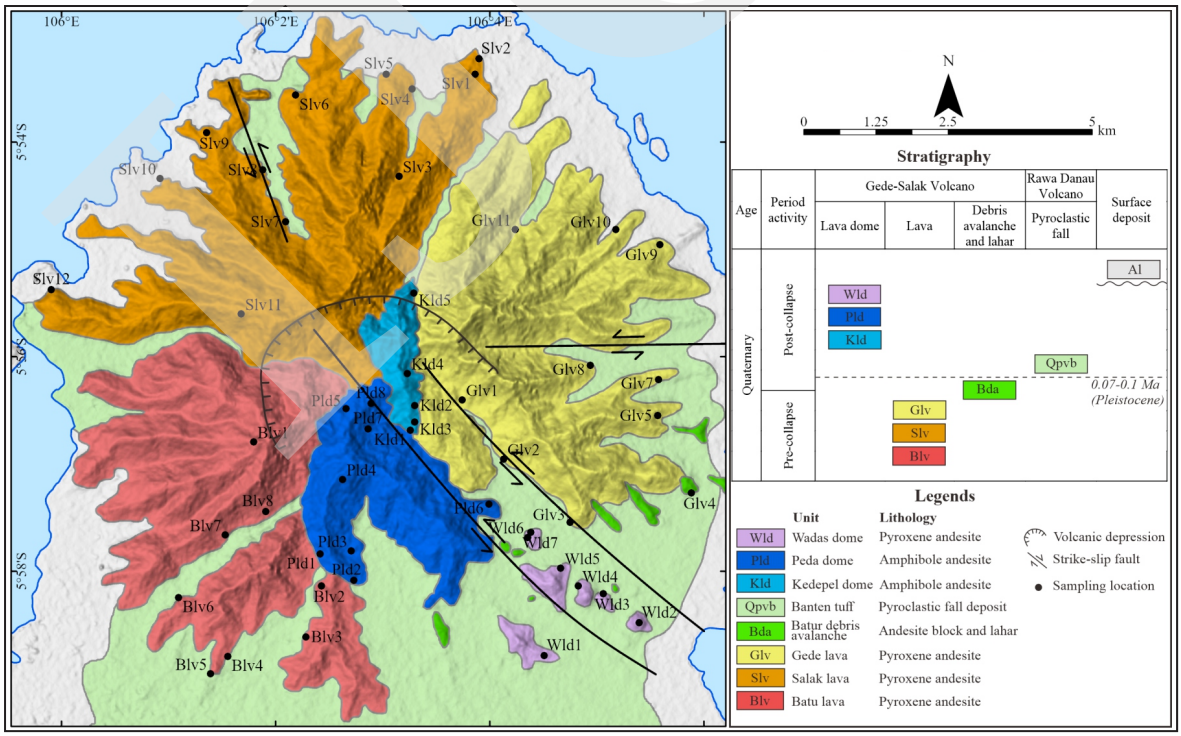


Figure 1. Geological map and stratigraphy of Gede-Salak Volcano.

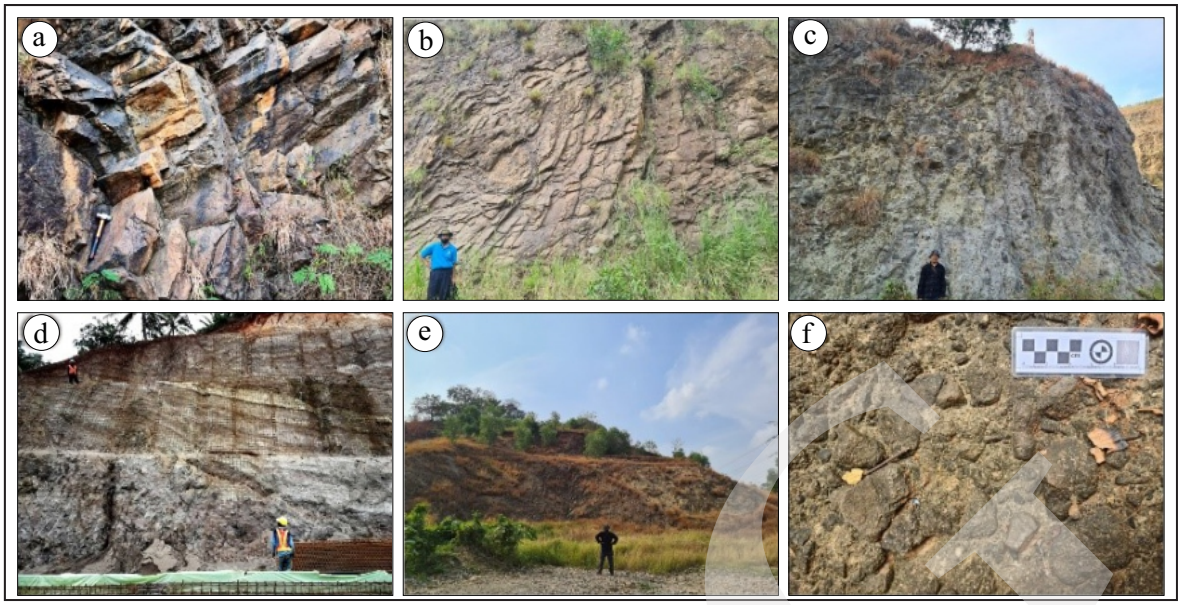


Figure 2. Photograph of (a) Prismatic joint in andesite outcrop of Batu lava, (b) Platy joint in andesite outcrop of Gede lava, (c) Debris avalanche deposit, (d) Banten tuff, (e) Small peripheral lava domes, and (f) Auto brecciated lava clinker.

pumice clasts ranging in grain size from centimeters to tens of meters (Figure 2c). It is often associated with the lahar deposit. Lahar deposit is poorly sorted, inversely graded, and consists of rounded to subangular andesite and pumice clast. Subsequently, pyroclastic fall deposits of Banten tuff from the neighbouring south volcano, Rawa Danau Caldera, are deposited. A well-stratified layer of pyroclastic fall deposits characterizes the unit (Figure 2d).

Development of lava domes characterized the latest volcanism (Figure 2e). Two summit domes are located in the centre of the volcano, namely Kedepel Dome (Kld) and Peda Dome (Pld). Andesitic dome displays columnar or prismatic and platy joints. A substantial part of the upper region of the lava dome features auto brecciated lava clinker (Figure 2f). As previously mentioned, the lava dome emplacement followed the NW-SE trend of fault structure.

## $SiO_2$ Contents and Classification

Common volcanic rocks classification, including Total Alkali Silica (TAS) diagram (Le Bas *et al.*, 1986) with alkali-subalkali boundary line (Irvine and Baragar, 1971), tholeiite-calc-alkaline (Miyashiro, 1974), AFM diagram (Irvine and Baragar, 1971), and magma affinity based on $K_2O$ content (Gill, 1981) were employed (Figure 3). The lava flow samples range from basaltic andesite to andesite (56-63% $SiO_2$). The summit dome samples range from basaltic andesite to dacite (56-64% $SiO_2$). A peripheral dome has a narrow range of andesite composition (59-62% $SiO_2$). Generally, Gede-Salak demonstrates calc-alkaline characteristics with low to medium K magma affinity.

## Major Elements and Trace Element Variation

Whole-rock geochemistry data of major and trace elements is presented in Table 2. Major elements are plotted against $SiO_2$ in variation diagrams (Figure 4). $Na_2O$ and $K_2O$ show a positive correlation against $SiO_2$, while MgO, $TiO_2$, CaO, and $FeO^t$ show a negative correlation. A few different trends are observed among the samples. The summit dome shows an increasing $Al_2O_3$ against $SiO_2$ with an inflection at ~60% $SiO_2$ before decreasing. The lava flow shows two linear trends of MgO and $Al_2O_3$ vs. $SiO_2$, which might indicate magma mixing.

Variation diagrams of selected Large-Ion Lithophile Elements (LILE) and High Field-Strength Elements (HFSE) are presented in Fig-

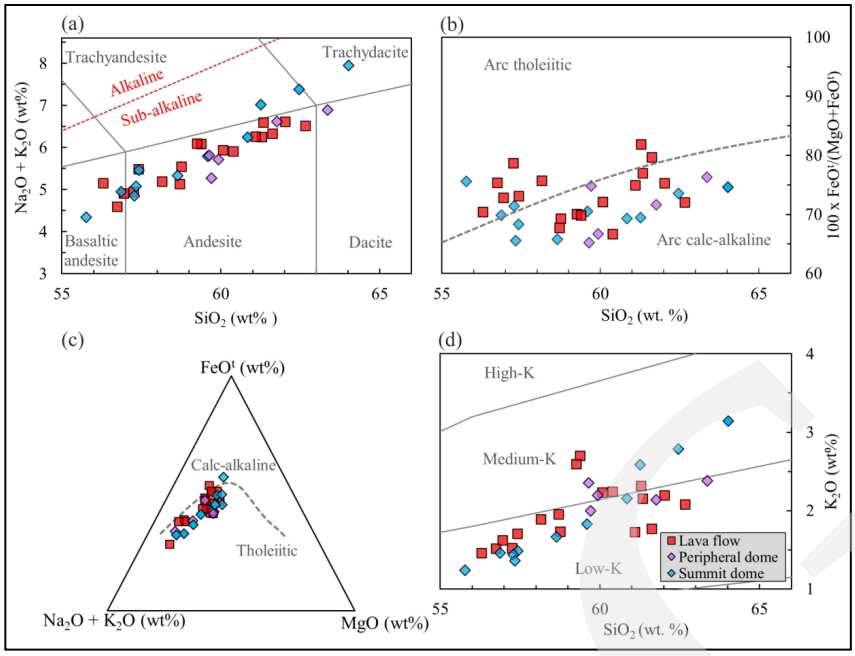


Figure 3. (a) TAS diagram (Le Bas *et al.*, 1986) with the boundary of alkali to subalkaline (Irvine and Baragar, 1971); (b) Tholeiitic and calc-alkaline boundary (Miyashiro, 1974); (c) Ternary diagram of AFM (Irvine and Baragar, 1971); and (d) Magma affinity (Gill, 1981).

ure 5. Rb, Pb, and Ba show an increasing trend against $SiO_2$, while Sr shows a decreasing trend with increasing $SiO_2$. Lava flows and peripheral dome have slightly higher Rb and Pb values than the summit caldera. The summit caldera shows an increasing trend of Sr with an inflection point at ~60% $SiO_2$ before starting to decrease. Ta, Zr, and Nb show a similar increasing trend in all samples. However, the summit dome showed an increasing trend in Hf *vs*. $SiO_2$.

## N-MORB Normalized Incompatible Trace Elements

Normalized variation diagrams evaluate the concentrations of selected incompatible trace elements against Normal Mid-Ocean Ridge Basalt (N-MORB) (Sun and McDonough, 1989) to emphasize enrichments in groups of mobile fluid elements such as LILE and Light REE (LREE) over less mobile groups of elements such as HFSE and Heavy REE (HREE). The profile of Gede-Salak shows a typical trend of subduction volcanic arc (Figure 6). The profile exhibits an increasing trend in element concentrations from Lu to Cs, punctuated by some positive anomalies at Sr, Pb, K, and Ba and equally significant negative anomalies for Nb and Ta.

Gede-Salak samples display higher values of LILE and HFSE compared to West Java Quaternary volcanoes, which are expected from the rear-arc volcano in West Java. Source enrichment of LILE and HFSE has been attributed to SED and AOC, which contributes greater toward the rear arc (Sendjaja *et al.*, 2009). Furthermore, northwest Java volcanoes generally have a slightly higher fluid contribution compared to the other rear-arc Quaternary West Java volcano (Kurniawan *et al.*, 2011, 2013).

## Chondrite-normalized Rare-Earth Elements

Normalized variation diagrams of REE against chondrite value (McDonough and Sun, 1995) are presented (Figure 7). The lava flow and summit dome show a subparallel pattern with greater REE content toward a more evolved sample within the same unit. Increasing Eu anomaly was also observed as the sample evolved. Meanwhile, summit dome samples showed a spoon-convex REE pattern characterized by Medium Rare Earth Element (MREE) depletion coupled

Table 2. Whole Rock Composition of Gede-Salak Volcano

| **Sample** | **Blv3** | **Blv4** | **Blv6** | **Blv7** | **Blv8** | **Slv1** | **Slv3** | **Slv4** | **Slv5** | **Slv6** | **Slv9** | **Slv11** |
|---|---|---|---|---|---|---|---|---|---|---|---|---|
| Major element, wt% | | | | | | | | | | | | |
| $SiO_2$ | 56.86 | 56.28 | 59.14 | 61.04 | 59.61 | 60.89 | 60.06 | 61.49 | 57.19 | 56.54 | 57.59 | 58.96 |
| $TiO_2$ | 0.96 | 0.98 | 0.86 | 0.96 | 0.83 | 0.64 | 0.82 | 0.71 | 0.78 | 0.89 | 0.84 | 0.84 |
| $Al_2O_3$ | 18.98 | 18.92 | 17.59 | 19.35 | 18.07 | 18.98 | 17.06 | 18.51 | 18.37 | 18.08 | 19.49 | 17.99 |
| $FeO^t$ | 8.17 | 8.18 | 6.93 | 4.56 | 6.44 | 5.09 | 6.51 | 5.10 | 8.11 | 8.76 | 6.75 | 6.78 |
| MnO | 0.25 | 0.13 | 0.16 | 0.04 | 0.12 | 0.11 | 0.11 | 0.08 | 0.13 | 0.14 | 0.11 | 0.15 |
| CaO | 6.69 | 7.09 | 5.49 | 5.40 | 5.31 | 5.22 | 5.55 | 4.83 | 6.28 | 6.37 | 6.66 | 5.55 |
| MgO | 2.21 | 2.67 | 2.99 | 1.17 | 2.49 | 1.52 | 3.25 | 1.67 | 2.98 | 3.27 | 2.17 | 2.89 |
| $Na_2O$ | 3.40 | 3.05 | 3.38 | 4.53 | 3.68 | 4.41 | 3.64 | 4.38 | 3.76 | 3.27 | 3.27 | 3.48 |
| $K_2O$ | 1.51 | 1.51 | 2.69 | 1.75 | 2.22 | 2.14 | 2.23 | 2.18 | 1.70 | 1.61 | 1.88 | 2.58 |
| $P_2O_5$ | 0.27 | 0.37 | 0.37 | 0.26 | 0.48 | 0.26 | 0.22 | 0.21 | 0.29 | 0.36 | 0.30 | 0.28 |
| LOI | 0.45 | 0.43 | 0.50 | 0.49 | 0.45 | 0.33 | 0.18 | 0.38 | 0.25 | 0.21 | 0.21 | 0.29 |
| $H_2O$ (-) | 0.06 | 0.18 | 0.26 | 0.34 | 0.81 | 0.85 | 0.54 | 0.33 | 0.55 | 0.72 | 1.07 | 0.82 |
| Trace elements (XRF), ppm | | | | | | | | | | | | |
| V | 49 | 24 | 21 | -85 | 38 | 10 | 52 | -1 | 21 | 47 | 5 | 41 |
| Cr | 16 | 8 | 13 | 17 | 9 | 14 | 16 | 8 | 14 | 13 | 9 | 12 |
| Ni | 0 | 2 | 1 | 3 | 3 | 3 | 7 | 5 | 2 | 2 | 3 | 4 |
| Rb | 37 | 32 | 60 | 41 | 63 | 56 | 57 | 52 | 40 | 36 | 42 | 57 |
| Sr | 617 | 599 | 489 | 552 | 498 | 561 | 471 | 521 | 575 | 547 | 560 | 512 |
| Y | 41 | 24 | 30 | 36 | 26 | 23 | 24 | 25 | 22 | 21 | 25 | 28 |
| Zr | 168 | 162 | 186 | 173 | 185 | 180 | 169 | 182 | 172 | 150 | 153 | 180 |
| Ba | 452 | 323 | 302 | 294 | 368 | 370 | 343 | 357 | 279 | 302 | 183 | 513 |
| Trace elements (ICP-MS), ppm | | | | | | | | | | | | |
| Nb | | 4.79 | 5.54 | | 5.64 | 4.86 | | | 5.05 | | 3.84 | 5.43 |
| Cs | | 0.67 | 2.40 | | 2.67 | 1.79 | | | 1.66 | | 1.82 | 2.33 |
| La | | 21.17 | 25.10 | | 23.82 | 18.85 | | | 21.13 | | 17.24 | 23.28 |
| Ce | | 44.48 | 52.68 | | 49.50 | 41.68 | | | 45.46 | | 34.60 | 49.33 |
| Pr | | 5.70 | 6.60 | | 6.35 | 5.24 | | | 5.79 | | 4.71 | 6.12 |
| Nd | | 23.94 | 27.06 | | 25.58 | 21.49 | | | 23.85 | | 20.13 | 24.83 |
| Sm | | 5.17 | 5.63 | | 5.31 | 4.49 | | | 4.88 | | 4.48 | 5.13 |
| Eu | | 1.56 | 1.50 | | 1.53 | 1.31 | | | 1.43 | | 1.33 | 1.46 |
| Gd | | 5.06 | 5.63 | | 5.06 | 4.30 | | | 4.68 | | 4.56 | 5.07 |
| Tb | | 0.73 | 0.83 | | 0.73 | 0.61 | | | 0.66 | | 0.67 | 0.74 |
| Dy | | 4.26 | 4.80 | | 4.17 | 3.53 | | | 3.78 | | 4.02 | 4.28 |
| Ho | | 0.87 | 0.98 | | 0.84 | 0.70 | | | 0.75 | | 0.82 | 0.87 |
| Er | | 2.57 | 2.95 | | 2.48 | 2.08 | | | 2.28 | | 2.42 | 2.63 |
| Tm | | 0.37 | 0.43 | | 0.36 | 0.30 | | | 0.33 | | 0.35 | 0.38 |
| Yb | | 2.55 | 3.02 | | 2.49 | 2.02 | | | 2.26 | | 2.40 | 2.63 |
| Lu | | 0.39 | 0.47 | | 0.36 | 0.29 | | | 0.34 | | 0.36 | 0.40 |
| Hf | | 3.15 | 4.14 | | 4.20 | 3.80 | | | 3.53 | | 3.20 | 4.02 |
| Ta | | 0.63 | 0.69 | | 1.07 | 0.89 | | | 0.80 | | 0.92 | 0.96 |
| Pb | | 6.68 | 10.03 | | 10.32 | 16.01 | | | 8.54 | | 7.61 | 9.86 |
| Th | | 4.13 | 7.05 | | 7.06 | 6.22 | | | 4.80 | | 4.73 | 6.83 |
| U | | 0.83 | 1.42 | | 1.55 | 1.27 | | | 1.00 | | 0.94 | 1.39 |
| **Sample** | **Slv12** | **Glv1** | **Glv3** | **Glv9** | **Glv10** | **Glv11** | **Kld1** | **Kld2** | **Kld3** | **Kld4** | **Kld5** | **Pld1** |
| Major element, wt% | | | | | | | | | | | | |
| $SiO_2$ | 58.48 | 58.33 | 60.66 | 56.00 | 62.20 | 60.85 | 56.75 | 58.09 | 56.52 | 55.76 | 57.04 | 61.18 |
| $TiO_2$ | 0.89 | 0.72 | 0.65 | 1.04 | 0.75 | 0.83 | 0.90 | 0.74 | 0.96 | 1.07 | 0.97 | 0.64 |
| $Al_2O_3$ | 17.65 | 17.78 | 19.44 | 18.75 | 20.29 | 18.43 | 18.56 | 18.61 | 18.04 | 17.91 | 18.24 | 19.19 |
| $FeO^t$ | 7.61 | 7.43 | 5.05 | 7.86 | 3.02 | 6.21 | 7.60 | 6.29 | 8.37 | 10.04 | 7.37 | 4.91 |
| MnO | 0.13 | 0.17 | 0.07 | 0.10 | 0.03 | 0.10 | 0.15 | 0.17 | 0.20 | 0.18 | 0.27 | 0.13 |
| CaO | 5.87 | 5.81 | 5.27 | 6.96 | 5.03 | 4.94 | 6.89 | 6.34 | 6.54 | 7.07 | 6.43 | 5.83 |
| MgO | 3.62 | 3.30 | 1.68 | 3.30 | 1.17 | 1.38 | 3.04 | 3.27 | 3.61 | 3.24 | 3.87 | 2.18 |

Table 2. Continued...

| Sample | Slv12 | Glv1 | Glv3 | Glv9 | Glv10 | Glv11 | Kld1 | Kld2 | Kld3 | Kld4 | Kld5 | Pld1 |
|---|---|---|---|---|---|---|---|---|---|---|---|---|
| Major element, wt% | | | | | | | | | | | | |
| $Na_2O$ | 3.17 | 3.79 | 4.51 | 3.68 | 4.41 | 3.91 | 3.38 | 3.63 | 3.47 | 3.10 | 3.70 | 4.11 |
| $K_2O$ | 1.95 | 1.72 | 1.71 | 1.45 | 2.07 | 2.30 | 1.43 | 1.65 | 1.45 | 1.24 | 1.35 | 2.16 |
| $P_2O_5$ | 0.25 | 0.23 | 0.26 | 0.34 | 0.31 | 0.34 | 0.37 | 0.27 | 0.22 | 0.37 | 0.25 | 0.23 |
| LOI | 0.27 | 0.21 | 0.11 | 0.11 | 0.25 | 0.45 | 0.43 | 0.15 | 0.24 | 0.50 | 0.45 | 0.36 |
| $H_2O$ (-) | 0.52 | 0.97 | 0.57 | 0.68 | 0.19 | 0.67 | 1.90 | 1.90 | 0.47 | 0.25 | 0.96 | 0.63 |
| Trace elements (XRF), ppm | | | | | | | | | | | | |
| V | 35 | 19 | 22 | 28 | -38 | 47 | 10 | -8 | 167 | 171 | 168 | 31 |
| Cr | 10 | 14 | 10 | 13 | 9 | 15 | 6 | 12 | 6 | 13 | 12 | 10 |
| Ni | 4 | 2 | 2 | 5 | 6 | 6 | 3 | 2 | 3 | 2 | 2 | 6 |
| Rb | 46 | 42 | 39 | 30 | 47 | 61 | 28 | 34 | 28.6 | 21 | 25 | 45 |
| Sr | 508 | 612 | 573 | 571 | 532 | 503 | 671 | 621 | 474 | 464 | 561 | 482 |
| Y | 23 | 23 | 23 | 22 | 24 | 22 | 19 | 16 | 18 | 21 | 17.9 | 16 |
| Zr | 159 | 150 | 161 | 142 | 166 | 184 | 192 | 144 | 141 | 134 | 144 | 178 |
| Ba | 299 | 289 | 369 | 248 | 292 | 403 | 328 | 321 | 239 | 246 | 355 | 443 |
| Trace elements (ICP-MS), ppm | | | | | | | | | | | | |
| Nb | | 4.30 | | 3.35 | 4.87 | | | 4.43 | | | 4.52 | 5.66 |
| Cs | | 1.21 | | 0.71 | 0.78 | | | 1.04 | | | 1.99 | 1.09 |
| La | | 19.29 | | 16.24 | 19.98 | | | 19.96 | | | 17.83 | 19.94 |
| Ce | | 42.03 | | 34.85 | 42.99 | | | 44.42 | | | 41.60 | 40.35 |
| Pr | | 5.26 | | 4.58 | 5.66 | | | 5.56 | | | 5.25 | 4.91 |
| Nd | | 21.60 | | 19.71 | 23.72 | | | 21.38 | | | 20.37 | 19.45 |
| Sm | | 4.47 | | 4.44 | 5.12 | | | 4.37 | | | 4.10 | 3.70 |
| Eu | | 1.33 | | 1.36 | 1.51 | | | 1.39 | | | 1.28 | 1.16 |
| Gd | | 4.27 | | 4.47 | 5.03 | | | 4.54 | | | 4.22 | 3.56 |
| Tb | | 0.62 | | 0.67 | 0.72 | | | 0.64 | | | 0.61 | 0.50 |
| Dy | | 3.51 | | 3.84 | 4.12 | | | 3.72 | | | 3.56 | 2.84 |
| Ho | | 0.72 | | 0.78 | 0.83 | | | 0.77 | | | 0.72 | 0.59 |
| Er | | 2.15 | | 2.25 | 2.39 | | | 2.26 | | | 2.09 | 1.74 |
| Tm | | 0.31 | | 0.31 | 0.34 | | | 0.32 | | | 0.31 | 0.25 |
| Yb | | 2.13 | | 2.11 | 2.23 | | | 2.29 | | | 2.12 | 1.81 |
| Lu | | 0.32 | | 0.32 | 0.32 | | | 0.35 | | | 0.33 | 0.27 |
| Hf | | 3.15 | | 2.94 | 3.70 | | | 2.91 | | | 3.15 | 3.48 |
| Ta | | 0.55 | | 0.79 | 0.97 | | | 0.38 | | | 0.37 | 0.77 |
| Pb | | 9.28 | | 6.76 | 10.68 | | | 7.15 | | | 5.22 | 9.23 |
| Th | | 5.02 | | 4.02 | 5.93 | | | 5.13 | | | 5.50 | 6.12 |
| U | | 1.01 | | 1.07 | 1.17 | | | 1.03 | | | 1.11 | 1.13 |

| Sample | Pld3 | Pld5 | Pld6 | Pld7 | Pld8 | Wld1 | Wld2 | Wld3 | Wld5 | Wld7 |
|---|---|---|---|---|---|---|---|---|---|---|
| Major element, wt% | | | | | | | | | | |
| $SiO_2$ | 60.81 | 59.13 | 57.16 | 61.91 | 63.42 | 63.06 | 61.94 | 59.99 | 59.18 | 59.47 |
| $TiO_2$ | 0.57 | 0.68 | 0.81 | 0.54 | 0.48 | 0.73 | 0.73 | 0.88 | 0.92 | 0.84 |
| $Al_2O_3$ | 19.25 | 19.16 | 18.64 | 18.83 | 17.91 | 18.48 | 17.74 | 17.31 | 18.05 | 17.34 |
| $FeO^t$ | 4.37 | 5.65 | 7.26 | 4.22 | 3.65 | 4.22 | 5.76 | 6.54 | 7.29 | 6.60 |
| MnO | 0.10 | 0.08 | 0.17 | 0.22 | 0.12 | 0.10 | 0.12 | 0.25 | 0.12 | 0.15 |
| CaO | 5.06 | 6.07 | 6.42 | 4.33 | 4.14 | 4.46 | 4.77 | 5.89 | 5.66 | 5.76 |
| MgO | 1.92 | 2.37 | 3.37 | 1.52 | 1.24 | 1.31 | 2.28 | 3.27 | 2.46 | 3.52 |
| $Na_2O$ | 4.40 | 3.94 | 3.96 | 4.56 | 4.76 | 4.49 | 4.49 | 3.52 | 3.25 | 3.45 |
| $K_2O$ | 2.57 | 1.81 | 1.48 | 2.76 | 3.11 | 2.37 | 2.14 | 2.20 | 1.98 | 2.35 |
| $P_2O_5$ | 0.21 | 0.34 | 0.28 | 0.24 | 0.22 | 0.31 | 0.31 | 0.27 | 0.22 | 0.22 |
| LOI | 0.17 | 0.37 | 0.43 | 0.42 | 0.26 | 0.29 | 0.37 | 0.33 | 0.32 | 0.31 |
| $H_2O$ (-) | 0.45 | 0.56 | 0.49 | 0.80 | 1.15 | 0.47 | 0.25 | 0.96 | 0.50 | 0.63 |

Table 2. Continued...

| Sample | Pld3 | Pld5 | Pld6 | Pld7 | Pld8 | Wld1 | Wld2 | Wld3 | Wld5 | Wld7 |
|---|---|---|---|---|---|---|---|---|---|---|
| Trace elements (XRF), ppm | | | | | | | | | | |
| V | 17 | -24 | 16 | 11 | 29 | -40 | 31 | 56 | 10 | 32 |
| Cr | 18 | 14 | 10 | 14 | 14 | 13 | 20 | 20 | 13 | 9 |
| Ni | 4 | 3 | 3 | 5 | 2 | 5 | 5 | 5 | 4 | 4 |
| Rb | 55 | 38 | 29 | 62 | 67 | 59 | 55 | 68 | 48 | 91 |
| Sr | 370 | 604 | 556 | 355 | 309 | 503 | 519 | 499 | 509 | 494 |
| Y | 14 | 19 | 19 | 15 | 18 | 14 | 24 | 33 | 23 | 28 |
| Zr | 174 | 172 | 140 | 229 | 199 | 174 | 163 | 165 | 156 | 169 |
| Ba | 395 | 297 | 224 | 390 | 418 | 324 | 373 | 593 | 324 | 306 |
| Trace elements (ICP-MS), ppm | | | | | | | | | | |
| Nb | | 4.66 | 4.95 | | 5.98 | 5.44 | | 4.68 | | 4.98 |
| Cs | | 1.16 | 0.49 | | 2.54 | 0.66 | | 3.24 | | 6.66 |
| La | | 22.19 | 18.10 | | 27.33 | 23.74 | | 24.93 | | 21.07 |
| Ce | | 46.39 | 38.44 | | 51.57 | 47.78 | | 48.74 | | 44.44 |
| Pr | | 5.83 | 4.96 | | 6.28 | 6.03 | | 6.16 | | 5.37 |
| Nd | | 22.11 | 20.97 | | 24.01 | 24.87 | | 25.09 | | 21.45 |
| Sm | | 4.38 | 4.53 | | 4.06 | 5.30 | | 5.05 | | 4.36 |
| Eu | | 1.35 | 1.42 | | 1.22 | 1.56 | | 1.50 | | 1.27 |
| Gd | | 4.23 | 4.51 | | 3.82 | 5.24 | | 5.43 | | 4.27 |
| Tb | | 0.61 | 0.66 | | 0.52 | 0.75 | | 0.77 | | 0.61 |
| Dy | | 3.50 | 3.87 | | 3.00 | 4.33 | | 4.61 | | 3.58 |
| Ho | | 0.75 | 0.80 | | 0.62 | 0.89 | | 0.97 | | 0.72 |
| Er | | 2.18 | 2.38 | | 1.86 | 2.61 | | 2.87 | | 2.15 |
| Tm | | 0.32 | 0.34 | | 0.28 | 0.38 | | 0.42 | | 0.32 |
| Yb | | 2.16 | 2.34 | | 2.04 | 2.51 | | 2.80 | | 2.23 |
| Lu | | 0.34 | 0.36 | | 0.32 | 0.37 | | 0.43 | | 0.34 |
| Hf | | 3.35 | 2.88 | | 3.76 | 3.89 | | 3.58 | | 3.69 |
| Ta | | 0.65 | 0.46 | | 0.88 | 1.04 | | 0.80 | | 0.98 |
| Pb | | 6.65 | 6.77 | | 10.86 | 12.21 | | 8.71 | | 9.50 |
| Th | | 5.25 | 4.67 | | 7.72 | 7.92 | | 6.53 | | 6.93 |
| U | | 1.07 | 0.93 | | 1.52 | 1.64 | | 1.56 | | 1.55 |

with LREE and HREE enrichment that became more prominent as the sample evolved.

## Petrographical Feature of Phenocrysts

Lava flow and peripheral dome exhibit similar petrographical features. Phenocrysts of plagioclase, orthopyroxene, clinopyroxene, and Fe-Ti oxides are abundant, with total ranges from 38 to 58 % by volume (Table 3). The samples contain accessory minerals of apatite. Phenocryst minerals can be found as both single crystals and glomerocryst aggregates. Typically, the aggregates consist of orthopyroxene, clinopyroxene, apatite, and Fe-Ti oxide. The groundmass has a hyalopilitic texture that is homogenous and predominantly made of glass, with trace amounts of plagioclase and pyroxene. Meanwhile, the presence of amphibole phenocryst distinguishes summit dome from lava flow and peripheral dome. The groundmass of the summit dome also features a distinct trachytic texture and is mainly composed of plagioclase microlites.

Plagioclase phenocrysts show a subhedral to euhedral shape with a maximum size of 5 mm. The phenocrysts are characterized by patchy (Figure 8a) or coarse-sieved cores (Figure 8b). Melt inclusions are found in coarse sieved cores and commonly include glass, pyroxene, and oxide minerals. Resorption surfaces are typical in the core and rim overgrowth, characterized by unconformable or irregular surfaces dissecting the growth bands discordantly (Figure 8c). Oscillatory zoning shows multiple dissolution-overgrowth textures within

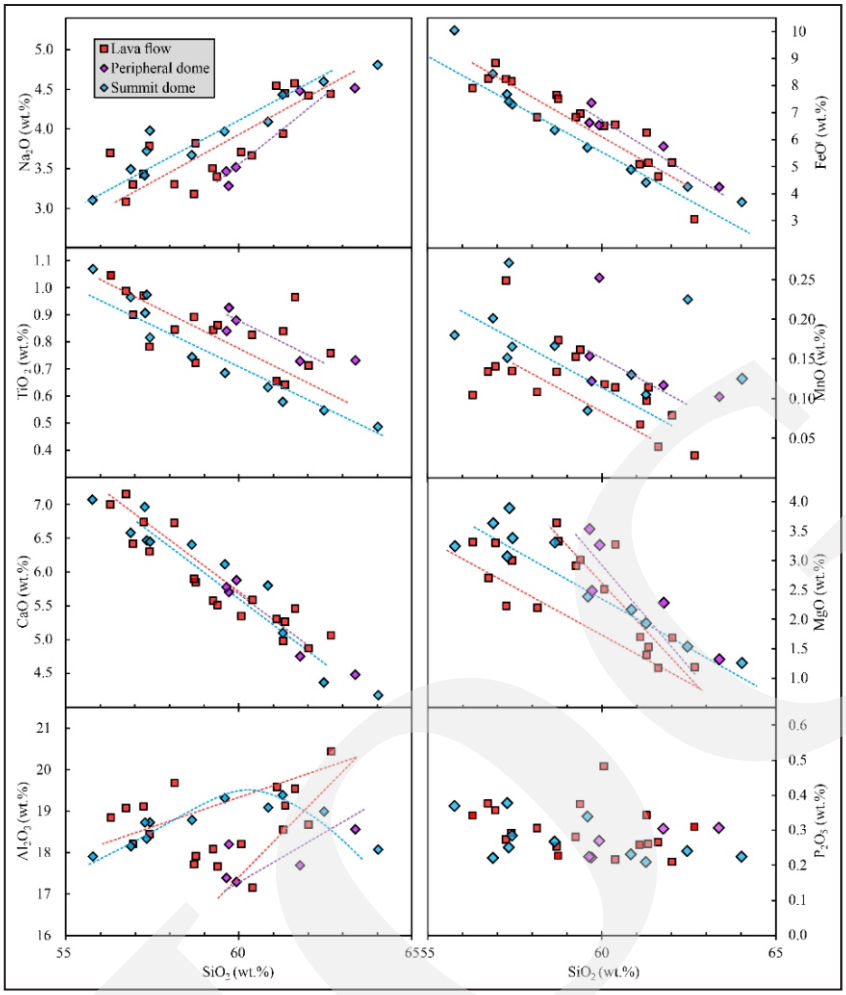


Figure 4. Variation diagrams of $SiO_2$ *vs.* selected major elements of Gede-Salak Volcano.

Table 3. Mineral Assemblage of Representative Samples Based on 1000-Point Counting

| Unit | | Sample | Gm (vol.%) | Phenocryst | | | | | $SiO_2$ (wt.%) | Rock Name |
|---|---|---|---|---|---|---|---|---|---|---|
| | | | | Pl | Cpx | Opx | Ox | Amp | | |
| Peripheral dome | Wadas | Wld1 | 42.3 | 52.1 | 1.2 | 3.2 | 1.2 | 0 | 63.06 | Px andesite |
| | | Wld7 | 40.6 | 50.5 | 1.9 | 5.2 | 1.8 | 0 | 59.47 | Px andesite |
| Summit Dome | Peda | Pld5 | 63.3 | 22.9 | 0.4 | 1.5 | 1.4 | 10.5 | 59.13 | Hbl andesite |
| | | Pld6 | 62.1 | 19.7 | 0.9 | 2.4 | 2.5 | 12.4 | 57.16 | Hbl andesite |
| | Kedepel | Kld2 | 65.1 | 19.2 | 0.8 | 2.6 | 2.1 | 10.2 | 57.29 | Hbl andesite |
| Lava flow | Gede | Glv1 | 54.6 | 38.1 | 2.1 | 3.9 | 1.3 | 0 | 58.33 | Px andesite |
| | | Glv9 | 52.8 | 36.5 | 2.9 | 5.5 | 2.3 | 0 | 56 | Px andesite |
| | Salak | Slv6 | 61.2 | 28.7 | 2.7 | 5.3 | 2.1 | 0 | 56.54 | Px andesite |
| | | Slv11 | 65 | 27.8 | 1.8 | 4.2 | 1.2 | 0 | 58.96 | Px andesite |
| | Batu | Blv3 | 54.7 | 39.2 | 2.3 | 3 | 0.8 | 0 | 56.86 | Px andesite |
| | | Blv8 | 53 | 41.3 | 1.7 | 3 | 1 | 0 | 59.61 | Px andesite |

its growth (Figure 8a). Orthopyroxene is commonly more abundant and bigger (<2 mm) than clinopyroxene (<1 mm). Both homogeneous and zoned pyroxene phenocrysts are present. Homogenous pyroxene is typically found as part of the glomerocryst (Figure 8d). Some zoned pyroxene develops oscillatory zoning (Figure 8e). Several orthopyroxenes show rounded and embayed cores

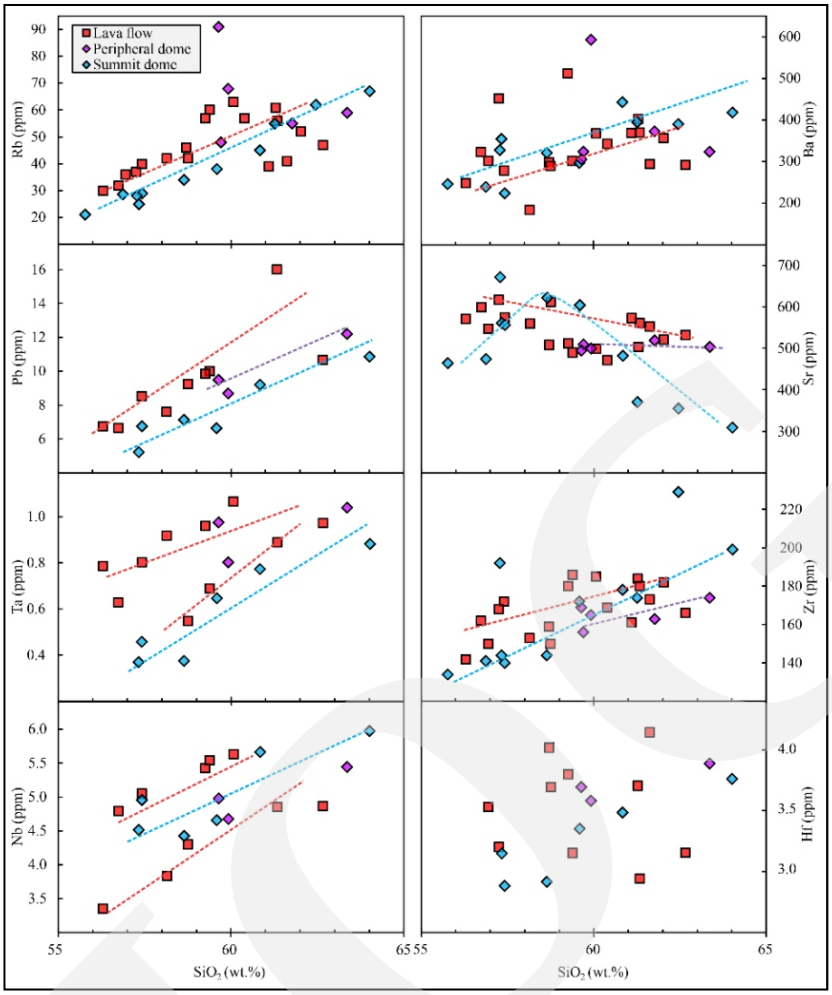


Figure 5. Variation diagrams of $SiO_2$ *vs.* selected LILE and HFSE of Gede-Salak samples.

that are mantled by clinopyroxene (Figure 8f), although the plagioclase texture of the summit dome is comparable to lava flow and peripheral dome. In contrast, pyroxene shows a distinct feature of a homogenous core that is mantled with a dusty texture rim (Figure 8g). Amphibole has a clear texture and an opacitic rim, as well as a volumetric breakdown (Figure 8h and 8i).

## Zoning, Texture, and Population Distribution of Phenocryst Chemistry

### *Plagioclase Phenocryst*

Distribution and zonation of plagioclase phenocryst are shown in Figure 9. Batu lava flow shows a unimodal distribution of An content centred at $An_{44}$. Meanwhile, Salak lava flow and peripheral dome (Wadas dome) show a trimodal distribution with multiple modes at $An_{44}$, $An_{60}$, and $An_{80}$. The summit dome (Peda Dome) exhibits bimodal distribution with modes at $An_{52}$ and $An_{84}$. The lava flow and peripheral dome show reverse and normal zoning. In contrast, the summit dome sample is dominated by normally zoned plagioclase.

Representative plagioclases were examined as BSE images along with their An and FeO profiles along a straight path (Figure 10). Following Viccaro *et al.* (2010), a concordant behaviour is when the An content increases and FeO increases or vice versa for each spot analyses along the same direction, independent of the absolute extent of the variation. Conversely, the discordant behaviour is when An increases and FeO decreases or remains constant.

Type 1 plagioclases are characterized by a low amplitude oscillatory zoning of low-An core ($An_{48-50}$) interrupted by a resorbed surface. The

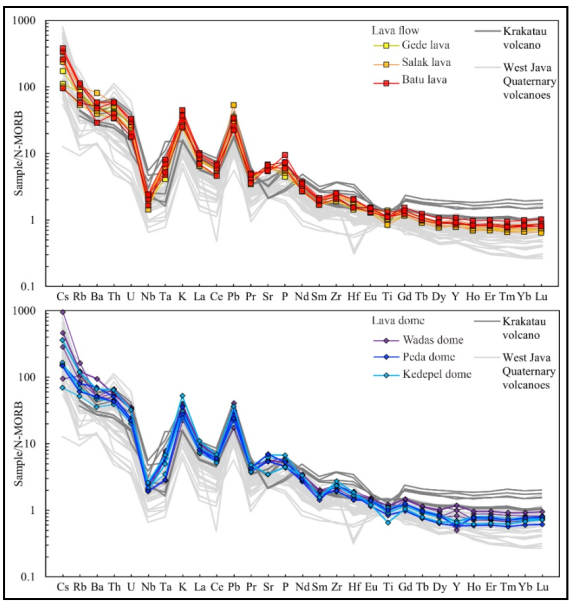


Figure 6. N-MORB normalized multi-element diagrams of Gede-Salak samples.

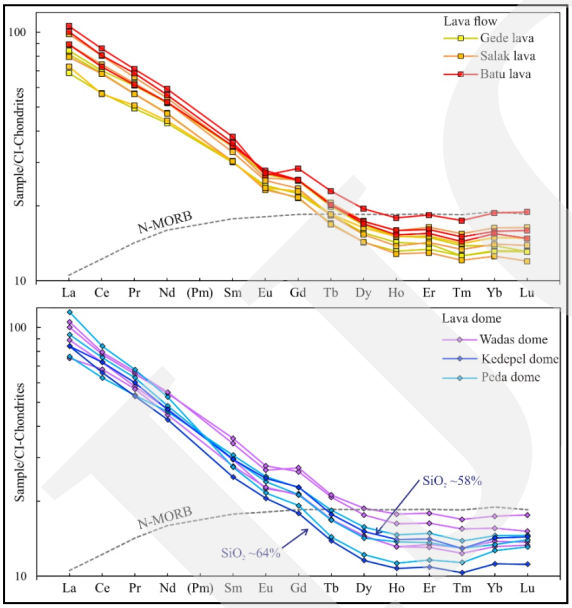


Figure 7. Chondrite normalized REE diagrams of Gede-Salak samples.

resorbed surface is enveloped by high-An mantle ($An_{60-70}$) and concordant FeO enrichment that marked the beginning of high amplitude oscillatory zoning. Most type 1 plagioclase shows two to three cycles of oscillatory zoning overgrowth. The resorption surface separated each cycle. Type 2 plagioclase displays a strongly resorbed ovoidal core of high-An ($An_{\sim80}$) followed by an abrupt decrease in An ($An_{\sim55}$) and FeO marks the edge of the ovoidal core. Type 2 plagioclase is commonly preceded by a multiple dissolution-overgrowth of high amplitude oscillatory zoning similar to type 1.

Type 3 plagioclases show a coarse sieve texture of high-An cores ($An_{\sim80}$). These crystals possess numerous melt inclusions and microlites of Fe-Ti oxides. Coarse sieve texture typically shows a discordant trend of FeO. A thin outer rim envelops the core (<100 μm wide), displaying a normally zoned rim. Type 4 plagioclase displays patchy zoning of high-An core ($An_{\sim80}$) and low-An core ($An_{\sim40}$). The core is dissected by a major resorbed surface and often shows embayment. Type 4 plagioclase has a thin outer rim (<100 μm wide) that exhibits a normally zoned rim.

### *Pyroxene Phenocryst*

Clinopyroxene in Gede-Salak Volcano is classified as augite. Distribution and zonation of clinopyroxene are shown in Figure 11. Batu lava sample shows a unimodal distribution of augite with a mode of $Mg\#_{72}$. A similar distribution was found in Salak lava and the peripheral dome. Summit dome shows a slightly higher mode of $Mg\#_{76}$.

Orthopyroxene of Gede-Salak sample is classified as enstatite. The distribution and zonation of orthopyroxene composition are shown in Figure 12. Batu lava sample shows a unimodal population centred in $Mg\#_{64}$, while Salak lava and peripheral dome show a bimodal distribution with an additional high-Mg# population at $Mg\#_{74}$. The summit dome shows the unimodal distribution of centred at $Mg\#_{74}$. All sample exhibits pyroxene with clear and zonation texture. Pyroxene generally displays reverse and normal zoning in lava flow and peripheral dome. Meanwhile, most pyroxene in the summit dome shows either clear or normal zoning.

Representative textures of pyroxene from petrographic analyses are depicted in Figures 13 and 14. Type 1 pyroxene consists of progressive reverse zoning interrupted by resorbed surface and overgrowth of step reverse zoning. Progressive zoning produces smooth profiles where composi-

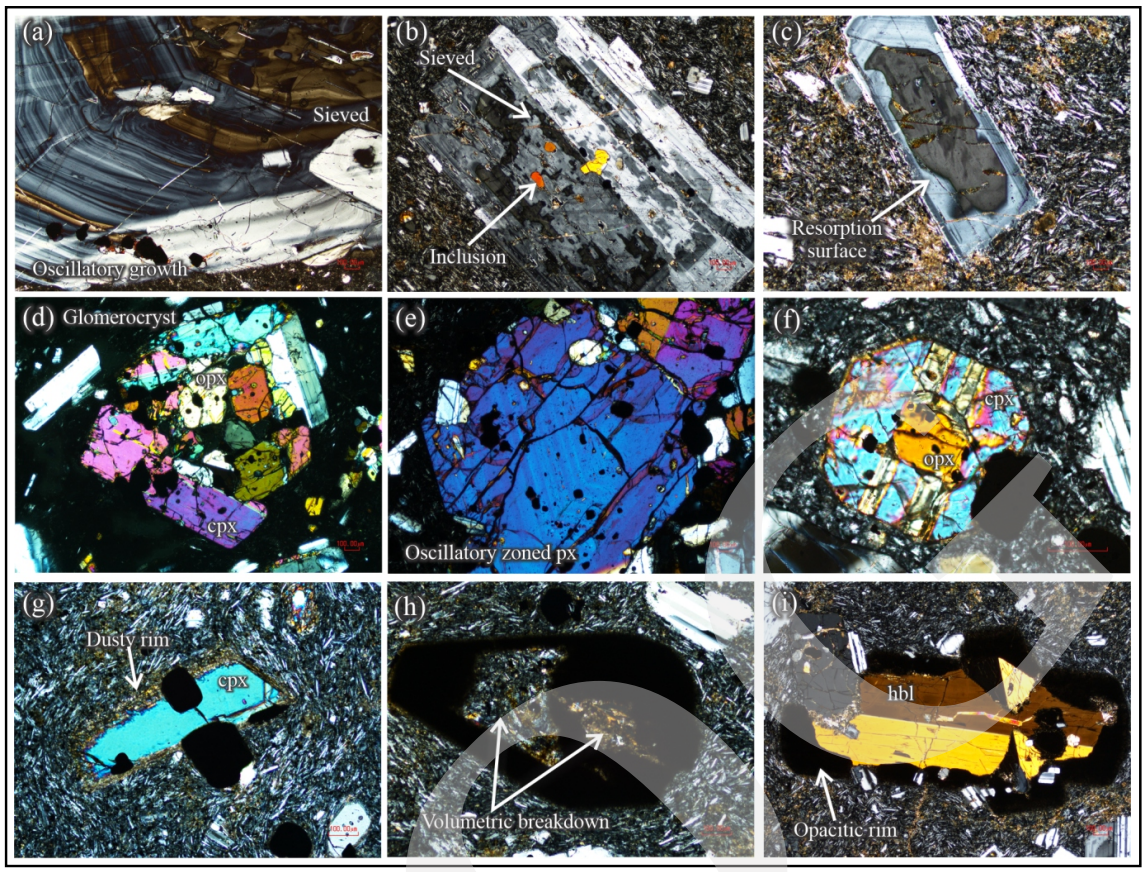


Figure 8. Representative photomicrographs of phenocryst texture and zonation: (a) Patchy core with multiple dissolution-overgrowth, (b) Coarse sieved core with melt inclusion, (c) Clear plagioclase with a resorbed surface, (d) Glomerocryst, (e) Oscillatory zoned pyroxene, (f) Rounded orthopyroxene mantled by clinopyroxene, (g) Clinopyroxene with spongy texture rim, (h) Amphibole with volumetric decomposition, and (i) Clear amphibole and plagioclase aggregate.

tions progressively change with position along an analyses profile, while step zoning forms discrete compositional steps. Type 2 pyroxene shows a rounded core overgrown by coarse oscillatory zoning. Occasionally, type 2 shows orthopyroxene that is mantled by clinopyroxene.

Type 3 pyroxene consists of homogenous to slightly normal zoning of high-Mg# ($Mg\#_{\sim 74}$) core in both clinopyroxene and orthopyroxene. This type 3 pyroxene is typically found as part of glomerocryst. Type 4 pyroxene is exclusive to the pyroxene of summit dome ($Mg\#_{\sim 74}$), characterized by its dusty rim. The dusty rim is encountered in the edge euhedral crystal and glomerocryst (Figures 14a and b). The symplectite texture of orthopyroxene and magnetite characterizes type 5 pyroxene (Figure 14c). Type 5 is only found as glomerocryst in lava flow and peripheral dome samples (Figure 14d).

### *Amphibole Phenocrysts*

Amphibole occurrence is limited to the summit dome sample. Based on IMA-recommended classification (Hawthorne *et al.*, 2012), amphiboles in the sample are classified as Ti-rich magnesio-hastingsite (Mg-hast). Amphibole shows a narrow range of Mg# value (Mg#66-70) and homogenous unzoned core (Figure 15).

Amphiboles in the sample exhibit varying breakdown features. The breakdown feature in the sample is identified based on Plechov *et al.* (2008). Thin or unrimmed amphibole is commonly encountered in the evolved samples of summit dome (Figure 16a). The amphibole exhibits symplectite rims and detached rims (Figure 16b). Symplectite rims show interlaced streams of pl+px+Fe-Ti oxide that flow perpendicular to the crystal face. A sequence of px + pl + Fe-Ti followed by a px-rich zone near the

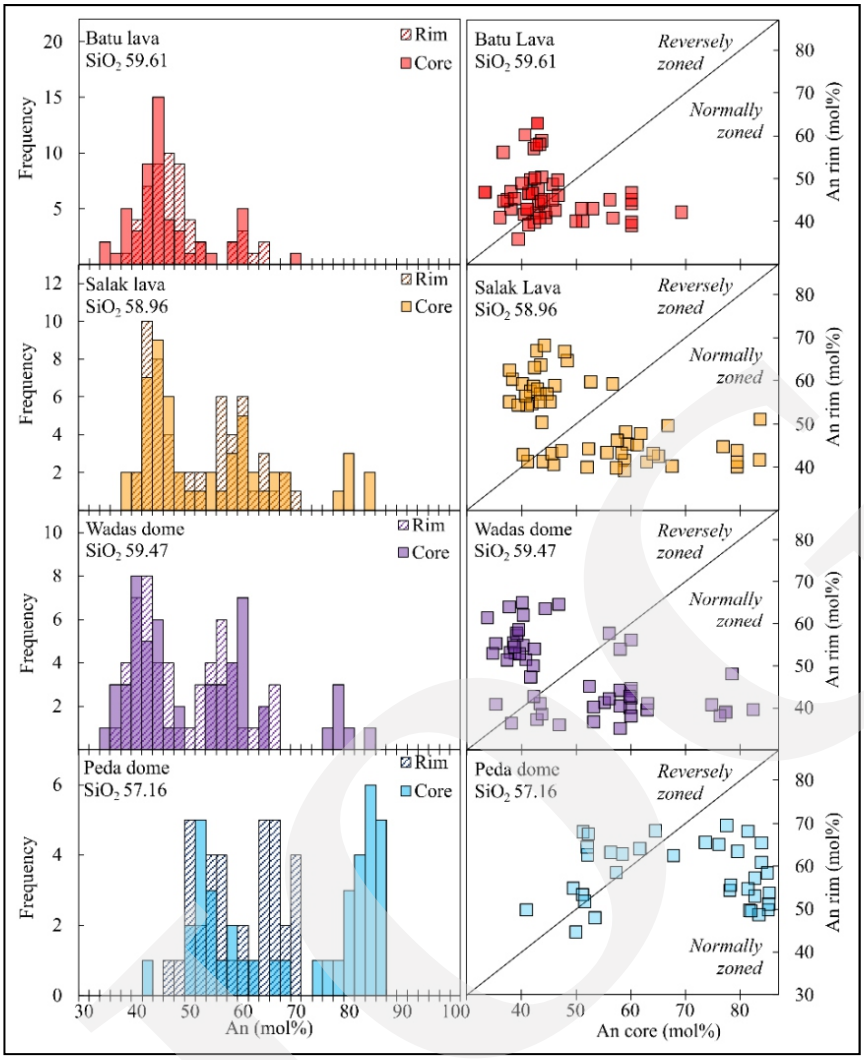


Figure 9. Distribution of composition in the rim and core of plagioclase.

groundmass is similar to the amphibole of the Bezymyannyi Volcano (Plechov *et al*., 2008). The outermost zone featured a thin px rim that floats in the melt and is often oriented parallel to subparallel to the crystal faces of the initial amphibole, which are referred to as detached rims (Figure 16b).

The breakdown feature of volumetric decomposition is characterized by the replacement of amphibole with aggregates of pl, px, and Fe-Ti oxide within the crystal. Volumetric decomposition is classified into irregular and aligned based on the mineral phases present and their habit. Irregular decomposition consists of anhedral grains of pl+px+Fe-Ti oxide occupying mineral fracture (Figures 16a, 16b, and 16c). Meanwhile, aligned decomposition shows euhedral, elongated grains in areas of pl + px (rare Fe-Ti oxide) occupying regions within the amphibole crystal (Figure 16d) (D'Mello *et al.*, 2021).

## Discussion

### Fractional Crystallization

Petrography and whole-rock geochemistry of Gede-Salak rocks inferred that the summit dome could be distinguished from the peripheral and lava flow. Amphibole is the predominant phenocryst in the summit dome compared to other units. Several trends in variation diagrams of major and trace elements highlight the summit dome distinctive

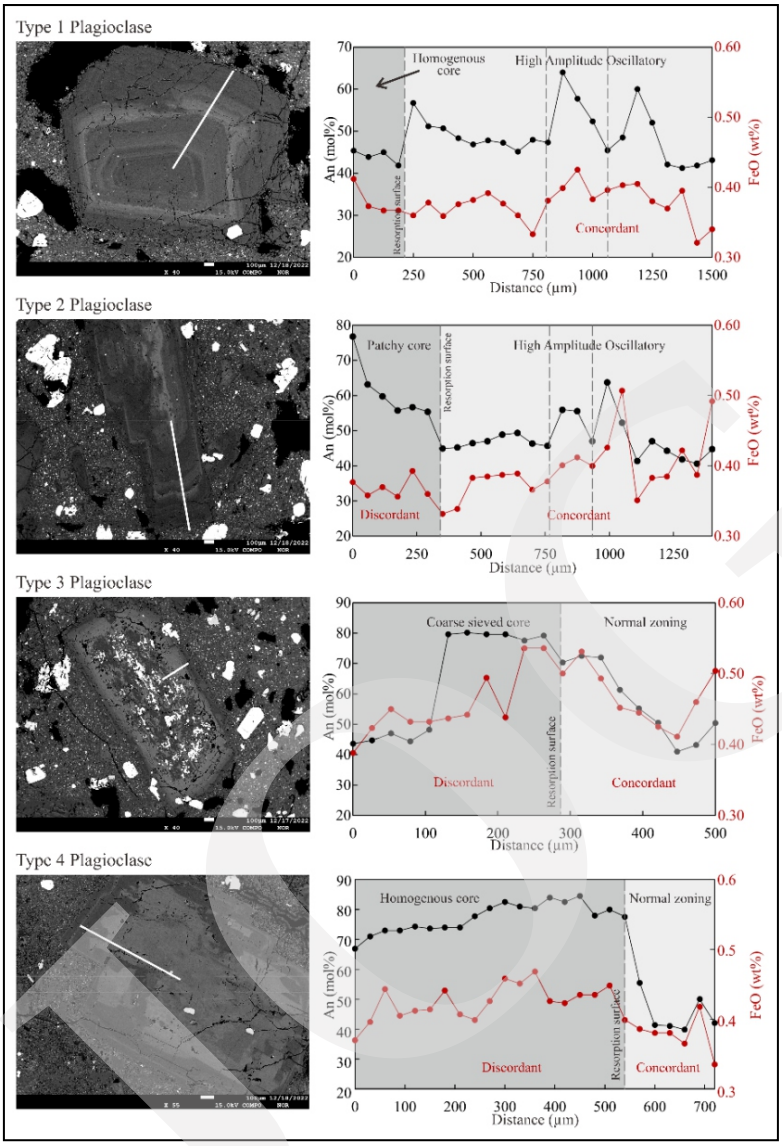


Figure 10. Representative BSE image and profile of typical plagioclase texture and zoning.

characteristics. In the meantime, the geochemical trends and mineral composition of the peripheral dome and lava flow showed an overlap. Therefore, for discussion, the lava flow and peripheral dome are referred to as magma type A, while the summit dome is called magma type B.

Several ratios, including K/Rb, Nb/Ta, Zr/Hf, and Sr/Y against $SiO_2$ are used to ascertain amphibole fractionation effects and overall geochemical distinction (Figures 17a-17d). Generally, the ratio shows a distinct trend between magma type A and type B. According to findings, K/Rb ratios in calc-alkaline arc lava are proportional to the modal amphibole content (Jakeš and White, 1970). Amphibole crystallization and removal contribute to a decreasing trend in the K/Rb ratio of arc magma (Green and Powell, 2006). The fractional crystallization of amphibole appears to control the increase in the bulk Nb/Ta fractionation trend of evolved hydrous arc magma (Green and Powell, 2006; Nandedkar *et al.*, 2016; Li *et al.*, 2017). Amphibole, clinopyroxene, and titanite will preferentially incorporate Hf over Zr, and the fractional crystallization of these minerals will therefore tend to increase the Zr/Hf ratio in the magmatic system residual melt (Linnen and Keppler, 2002). Intriguingly, the inflected trend of Sr/Y in amphibole-dominated fractionation is

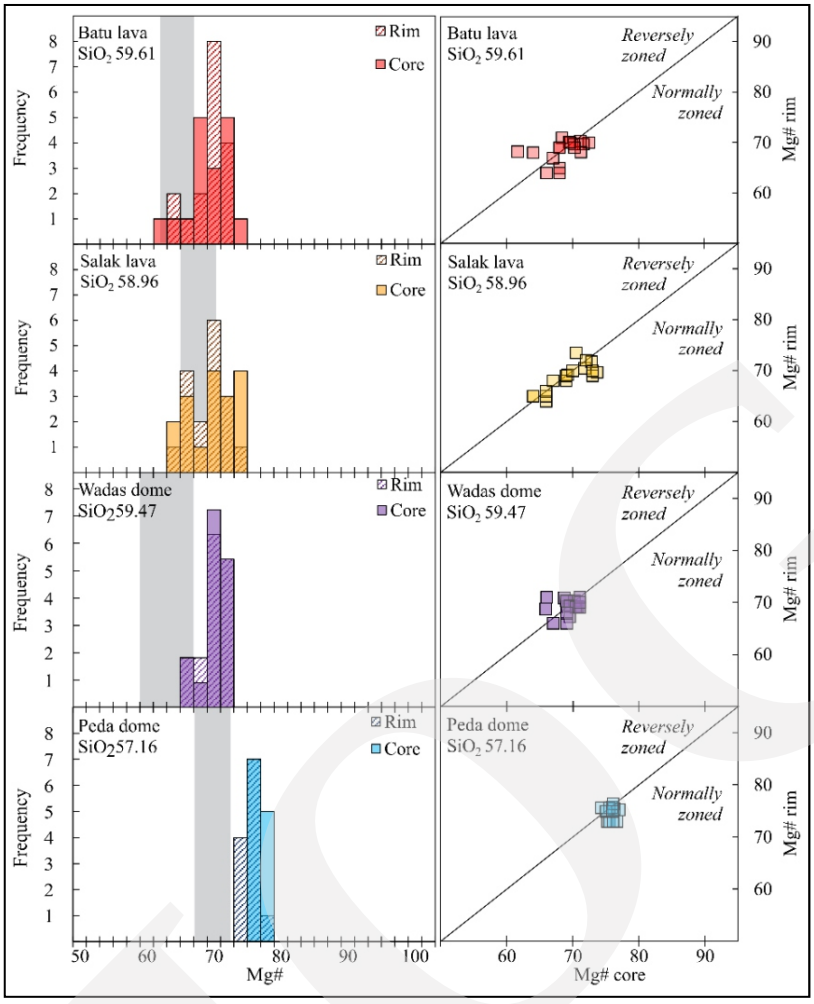


Figure 11. Distribution of composition in rim and core of clinopyroxene. Ranges of composition in equilibrium with each whole rock composition have been calculated utilizing $^{Fe\text{-}Mg}K_{Dmin/liq}$ values of 0.23-0.30 (Sisson and Grove, 1993).

observed experimentally (Nandedkar *et al.*, 2016) and naturally, Pre-Komitake lava (Shibata *et al.*, 2015), in hydrous arc magma. Early increase of Sr/Y is caused by Y strongly partitioned to amphibole (Davidson *et al.*, 2007; Kimura *et al.*, 2014). The subsequent decrease has been attributed to Sr partitioning to apatite or plagioclase in rhyolitic composition (Shibata *et al.*, 2015; Nandedkar *et al.*, 2016).

MREEs are favoured over HREEs in the composition of amphibole. Consequently, amphibole fractionation will raise the ratio of La/Yb and lower the ratio of Dy/Yb, as demonstrated in magma type B (Figures 17e and 17f) (Davidson *et al.*, 2007). Further consequent of fractional crystallization of amphibole-dominant systems results in a convex downward (spoon-shaped) pattern in the chondrite-normalized REE diagram (Figure 7) (Dessimoz *et al.*, 2012).

**Assimilation and Mixing**

Assimilation and magma mixing are identified in the evolution of magma in certain Sunda arc volcanoes. The ratio of K/Rb was chosen considering the correlation of this ratio to the wide range of $SiO_2$ in Gede-Salak and defining each magma type well. The ratio is proven helpful in monitoring crust-magma interaction in Sunda Arc, *e.g.* Salak (Handley *et al.*, 2007) and Sundoro (Wibowo *et al.*, 2022)), considering that magma and surrounding crust have distinctive values for the ratio (Hildreth and Moorbath, 1988). The ratio was plotted against Rb, representing the degree of magmatic differentiation. In Figure 18d, a straight

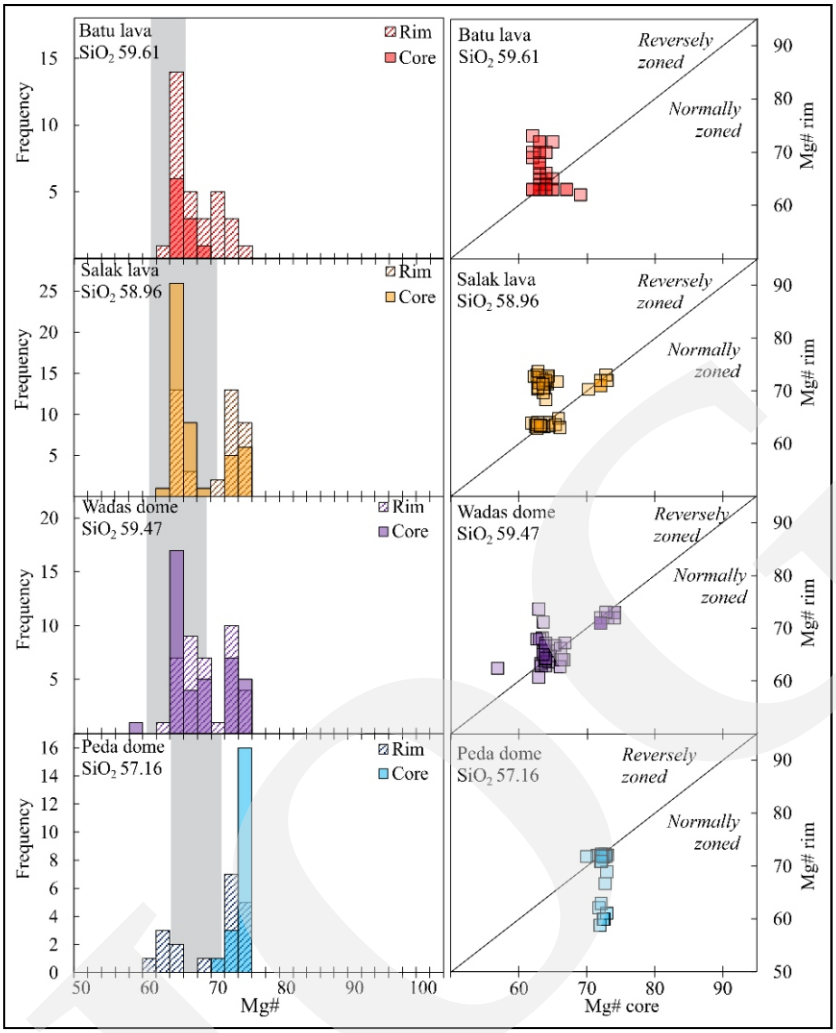


Figure 12. Distribution of composition in rim and core of orthopyroxene. Ranges of composition in equilibrium with each whole rock composition have been calculated utilizing $^{Fe\text{-}Mg}K_{Dmin/liq}$ values of 0.23-0.35 (Putirka, 2008).

pattern might indicate fractional crystallization, while a curved downward indicates the assimilation-fractional crystallization process (Handley *et al.*, 2008). Gede-Salak shows two distinct trends of the hyperbolic curve, which pointed toward the assimilation process. The process is supported by the occurrence of the crust-melt interaction feature, which will be discussed later.

As stated previously, the two linear trends of Nb, Ta, and MgO versus $SiO_2$ in the variation diagram of the lava flow sample indicate the magma mixing (Figures 18a-c). To further investigate the magma mixing, the diagram of K/Rb vs. Rb can be combined with the modal composition of the phenocrysts (Figure 18d) (Wibowo, 2017). As the sample differentiates in terms of Rb, the addition of higher-An plagioclase and higher-Mg# orthopyroxene become more prominent due to recharge by mafic magma. The diagram also implies that the mixing intensity increases from the older Gede lava to the younger Wadas Dome.

## Mineral Textures and Zoning as Evidence for Open System Processes

### *Implications of Texture and Zoning in Plagioclase Phenocrysts*

Low amplitude oscillatory zoning in the core (type 1) reflects incremental diffusion-controlled growth in equilibrium conditions during the steady cooling (Pearce, 1994; Ginibre *et al.*, 2002). Meanwhile, the rim displaying high am-

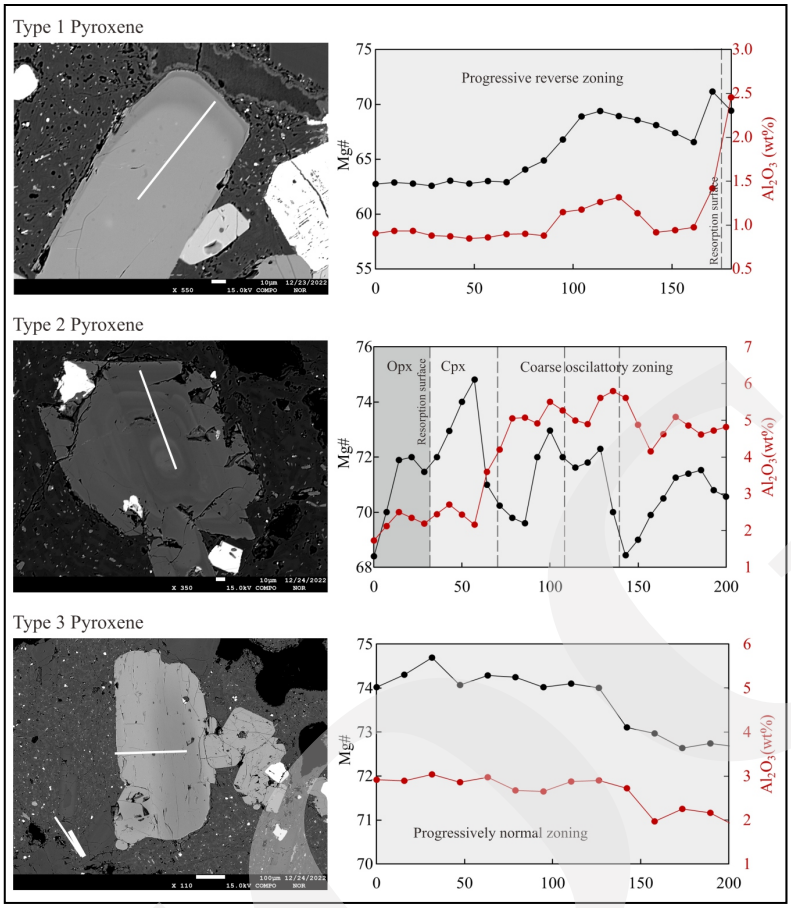


Figure 13. Representative BSE image and profile of pyroxene type 1, 2, and 3.

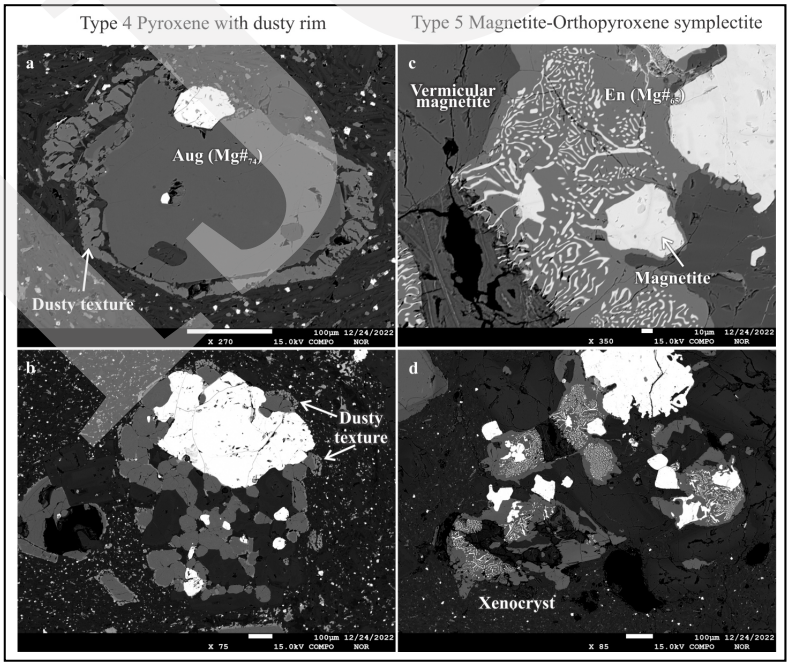


Figure 14. Photomicrograph of (a) Type 4 pyroxene displays a dusty rim, (b) Dusty rim restricted to part of glomerocryst that comes in contact with melt, (c) Type 5 pyroxene shows symplectite texture, and (d) Xenocryst showing the aggregate of symplectite texture.

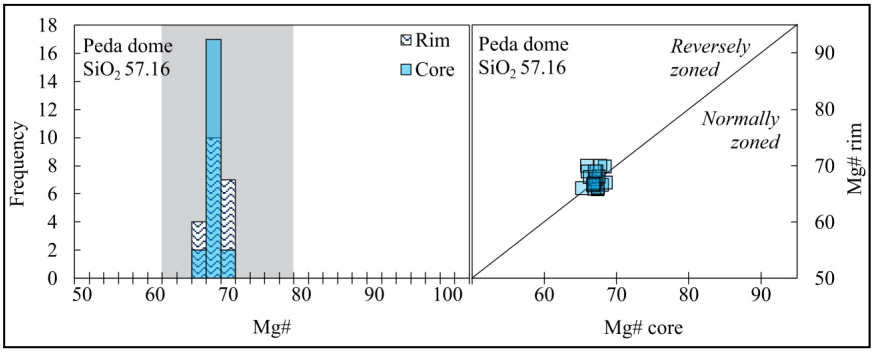


Figure 15. Distribution of composition in rim and core of amphibole.

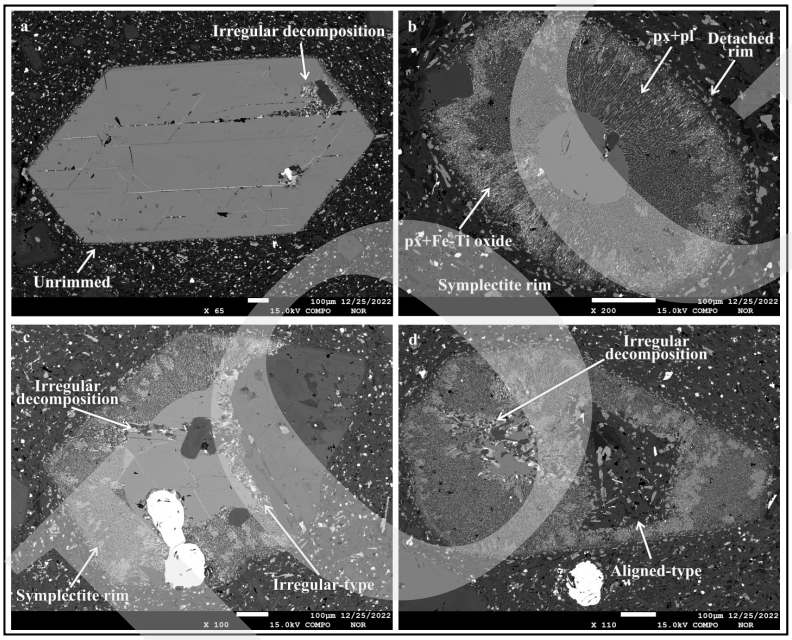


Figure 16. (a) Unrimmed amphibole displaying irregular decomposition, (b) Symplectite rim in amphibole showing zonation, (c) Irregular decomposition occupying fracture and mineral contact, and (d) Aligned decomposition occupying inner part of the amphibole.

plitude oscillatory rim (>10 An mol%) is more likely to reflect fluctuations in temperature, water pressure, or melt composition either from repeated magma recharge or crystal convection within a dynamic magma chamber (*e.g.* Viccaro *et al*., 2010; Coote and Shane, 2016). The rim is characterized by a rapid increase in An content when crossing a dissolution surface, followed by a progressive decrease before traversing the next dissolution surface, which results in the well-known sawtooth zoning pattern of plagioclase (*e.g.* Ginibre *et al*., 2002; Streck *et al*., 2008). Variable amplitude and frequency of oscillation response to thermally induced fluctuations by small, recurrent replenishments of less evolved, hotter magma (Streck *et al.*, 2008) as opposed to magma convection, which often results in a perfectly cyclic pattern of oscillations (Viccaro *et al.*, 2010). Additionally, concordant An-FeO behaviour of An-FeO throughout the zoning suggests the magma mixing (Ruprecht and Wörner, 2007). The type 1 plagioclase core is thought to have originated from felsic magma, and then received repeated mafic recharges during rim growth.

Strongly resorbed cores (type 2) are characterize by the irregular boundary of high-An content followed by low-An envelope. Significant compositional changes beyond the resorbed

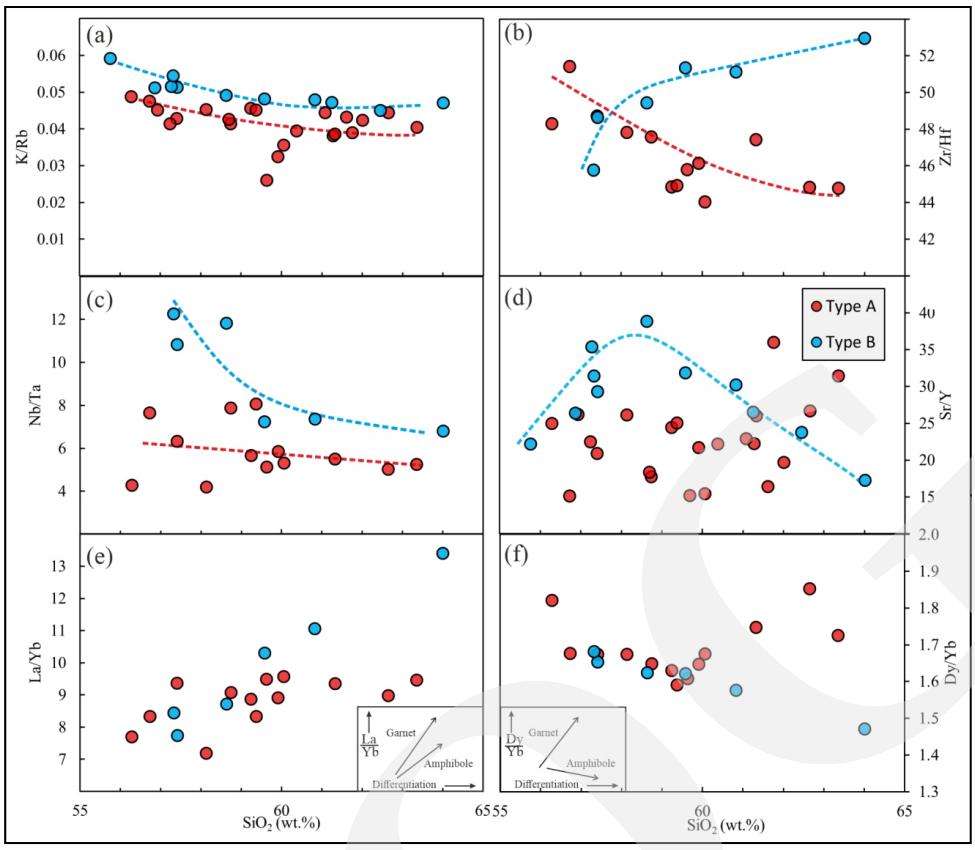


Figure 17. Amphibole fractionation effect on (a) K/Rb, (b) Zr/Hf, (c) Nb/Ta, (d) Sr/Y, (e) La/Yb, and (f) Dy/Yb *vs*. $SiO_2$. The schematic inset shows expected fractionation effects (Davidson *et al.*, 2007).

surface represent significant perturbations in the system physical and chemical characteristics. Undoubtedly, significant compositional changes beyond the resorbed surface represent significant perturbations in the system physically and chemically in which a portion of the crystal was dissolved or resorbed (Viccaro *et al.*, 2010). The texture might be acquired by a pressure decrease during fast ascent rates under $H_2O$-undersaturated conditions. P $H_2O$ of the system rises, drastically decreasing plagioclase stability and causing rapid dissolution (Blundy and Cashman, 2005; Cashman and Blundy, 2013). Typically, type 2 core is enveloped by a similar rim to the type 1 rim. Type 2 core is believed to have emerged from mafic magma that rapidly ascended to felsic magma and subsequently had identical rim growth to type 1 rim.

The patchy textured core (type 3) is resulted from the dissolution of An-poor plagioclase in irregular patches and the overgrowing of An-rich plagioclase or vice versa (*e.g.* Viccaro *et al.*, 2010; Cashman and Blundy, 2013; Coote and Shane, 2016). Several experimental outcomes indicate that at a given temperature, pressure decrease under $H_2O$-undersaturated conditions in a basaltic system lessens the plagioclase stability field and changes the composition toward relatively higher An (Hammer and Rutherford, 2002). Based on this evidence, type 3 core is viewed as the dissolution of pre-existing lower-An plagioclase, leaving uneven patches, and the growth of An-enriched plagioclase from the melt surrounding the dissolved crystal remains. The fact that the kinetics of such a process requires sufficient time to dissolve and precipitate suggests that magma ascent would not have been continuous and would have been significantly slower than the resorbed core outlined previously. Concordant An and FeO decrease at the edges might indicate that $H_2O$-saturation was finally reached in felsic magma, entailing the crystallization of a normally zoned

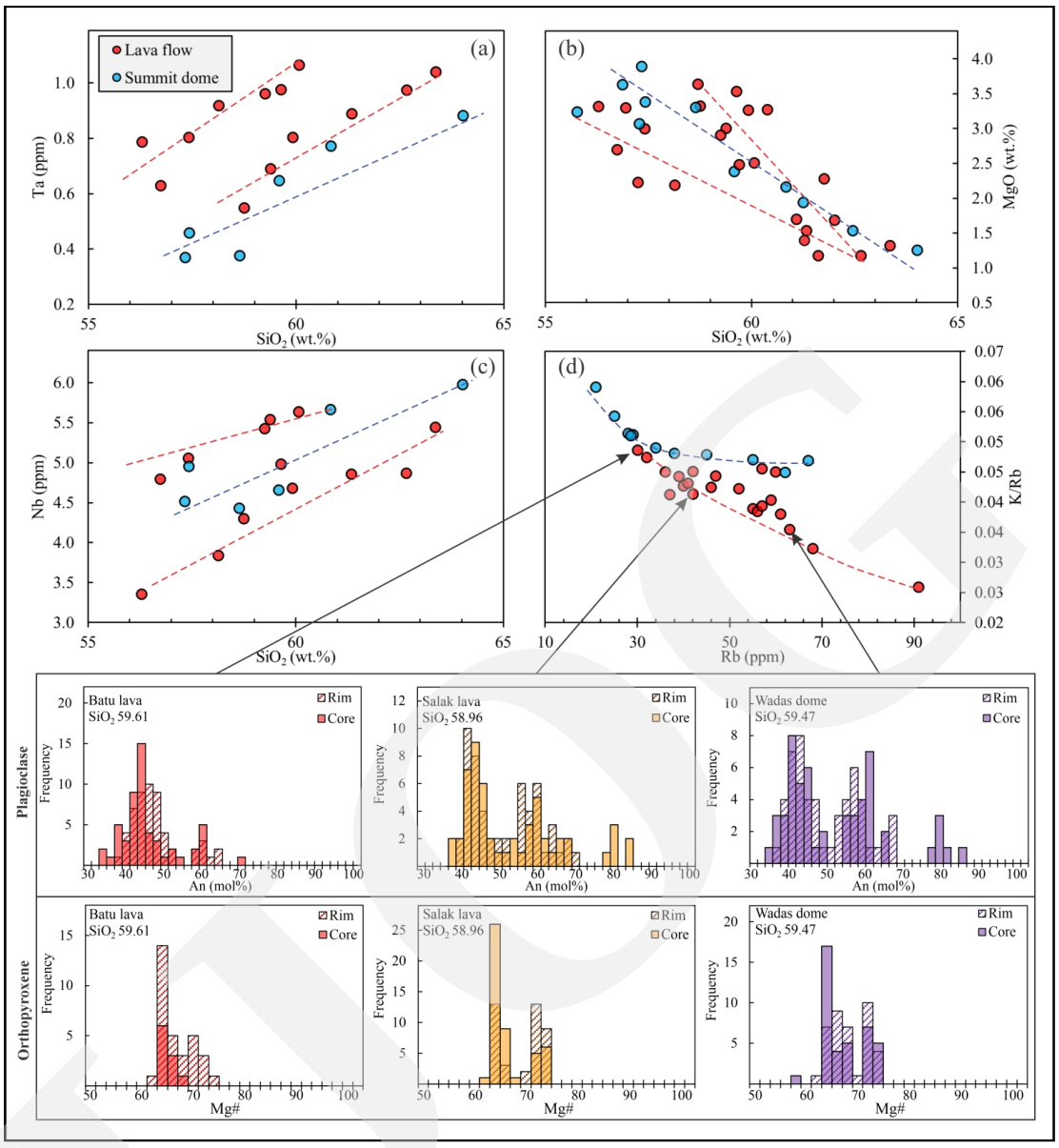


Figure 18. Indicator of mixing in whole rock and phenocryst composition. Two linear trends indicate mixing in (a) Ta, (b) Mg, and (c) Nb *vs*. $SiO_2$. The combination of (d) K/Rb *vs*. Rb and phenocryst composition suggests the magma mixing.

sodic rim (Viccaro *et al.*, 2010).

Coarse sieved core texture (type 4) can be acquired under similar circumstances to those described for types 2 and 3. Actuality, decompression under $H_2O$-undersaturated settings is able to destabilize plagioclase and, depending on ascent rates, produces diverse textures (Viccaro *et al.*, 2010). Given their textural characteristics, patchy and strongly resorbed cores can be regarded as end-members reflecting low and high ascent rates, respectively. The development of coarse sieve textures could therefore occur in decompression events with intermediate ascent rates between types 2 and 3.

### *Implications of Texture and Zoning in Pyroxene Phenocrysts*

Reverse zoning and resorption textures closely associated with step or progressive zoning (type 1) are rather prevalent in pyroxene. In many cases, these might be indicative of open system processes, such as magma replenishment and contamination, when taken in the context of compositional data of bulk rock (Streck, 2008).

Reverse zoning can appear as growth bands located anywhere from core to rim (*e.g.* Ohba *et al.*, 2007; Streck *et al.,* 2007). These growth bands have been interpreted to denote growth from more mafic magmas after previously growing from evolved magmas. The compositional changes associated with the growth bands typically occur in a step-zoning pattern. Prolonged entrainment could adjust the pattern to progressive zoning by diffusion (Costa *et al.*, 2008).

Fine-scale oscillatory zoning in pyroxene has been attributed to diffusion and nucleation rate, while coarse zoning in type 2 pyroxene (>15 μm) is a response to major changes in the physical and chemical conditions of the magma (Pearce, 1994; Ginibre *et al*., 2002). The changes are caused by either convection inside the dynamic magma chamber (Giacomoni *et al.*, 2016) or when a new batch of more primitive magma is injected into the chamber (Ginibre *et al.*, 2002; Streck *et al.*, 2007). To ensure that zoning corresponds to a more mafic input, Mg# should be concordant with changes in other cations such as Ti, Al, and Cr, as seen in Figure 13 (Cioni *et al.*, 1998; Streck, 2008). Additionally, the jagged and rounded surface between the zoning cycle is attributed to resorption when a new batch of more primitive magma is injected into the chamber (Pearce, 1994; Ginibre *et al.*, 2002).

Normal zoning (type 3) is characterized by compositional changes in the mineral from core to rim along the crystal growth stratigraphy, as would be generated by compositional changes in the melt as it follows a liquid line of descent during cooling. In a closed system, the changing mineral composition during crystallization mirrors the gradually evolving composition of the melt during solidification (Streck, 2008). In lava flow and peripheral dome, type 3 pyroxene is mainly encountered as glomerocrysts. However, in the summit dome, it occurs as both single crystals and glomerocrysts. It is hypothesized that type 3 pyroxene originates from closed, deeper mafic magma.

Dusty textures of type 4 pyroxene are unique to the summit dome. The texture develops in the rim of both individual crystals and glomerocryst. In glomerocryst, however, the texture is only present at the rim in direct contact with the melt. It stands to reason, as dusty textures indicate partial dissolution via reactivity with a Ca-richer and mafic magma. Dusty textures in pyroxene are the direct outcome of partial dissolution processes that emerge from an out-of-equilibrium interaction between a pre-existing core and a more mafic magma below the liquidus temperature (Giacomoni *et al*., 2016).

Magnetite-orthopyroxene symplectite (type 5) is exclusive to the lava flow and the periphery dome. The magnetite-orthopyroxene symplectite is commonly encountered in crustal olivine gabbro. Olivine oxidation occurs in lower crustal gabbro due to interaction with melt yields intergrowth of enstatite and magnetite (Efimov and Malitch, 2012), typically at 662-951°C and 1-4.64 kbar, according to two pyroxene geothermometry (Habtoor *et al.*, 2022). It is presumed that symplectite in the lava flow and peripheral dome is xenocryst incorporated from crustal gabbro. Two pyroxene geothermometry measurements of type 5 pyroxene yield an average of 916°C and 3.97 kbar.

***Implication of Amphibole Breakdown Feature***

Amphiboles from Gede-Salak without significant rim formation are the sole population in more felsic samples. The observations are comparable to amphiboles in the Augustine Volcano (De Angelis *et al.*, 2013). At Augustine, rim-free amphiboles were discovered in high silica andesites that exhibited little or no evidence of storage region disequilibrium, indicating low-temperature melts with high viscosity and that short ascent periods resulted in a negligible reaction.

The detached rims are commonly encountered in amphiboles [*e.g.* Bezymianny Volcano (Plechov *et al.*, 2008); experimental amphibole (De Angelis *et al.*, 2015); Taranaki Volcano (D'Mello *et al.*, 2021)]. The rim was attributed to a small but significant temperature increase within the amphibole stability field. D'Mello *et al.* (2021) suggest that the detached rim always initiates any amphibole breakdown when the

crystals are entrained in ascending, hot, low-viscosity melt presence. Likewise, the detached rim preceded every symplectite rim in the sample of the summit dome.

Symplectite rims were previously considered late-stage (syn-or post-eruption) oxidation-dehydrogenation reactions of the amphiboles (Plechov *et al*., 2008). In these researches, rims are observed in every crystal section and fracture. The symplectite rims in Gede-Salak differ due to the absence of rim formation when the amphibole crystal is in contact with other minerals or fractures, particularly in comparison to the Taranaki. It suggests that the symplectite rims resulted from the magmatic reaction between an unstable amphibole and its host melt, as opposed to a late-stage product of eruption-related decompression (D'Mello *et al.*, 2021).

Volumetric decomposition has been described to form by the open system processes. Aligned decompression resembles the breakdown documented by De Angelis *et al.* (2015), in which elongated px + pl (oxide poor) replaces amphibole when heated beyond the stability limit experimentally. In contrast, irregular decomposition results from the reaction of interstitial melt trapped in fracture and amphibole during ascent-related decompression (D'Mello *et al.*, 2021). Evidently, irregular decompression only developed in the presence of fractures and mineral grain contact (Figures 16a, 16c, and 16d). Moreover, irregular decomposition was also observed in unrimmed amphibole, indicating equilibrium magma condition, while aligned decomposition is always associated with symplectite rim (Figure 16d).

**Origin of Phenocrysts**

Compositional variations of the phenocrysts determine the origin of the phenocrysts. The assemblages of early-formed crystals in magma are established by finding the mutual chemical equilibrium among mineral and whole-rock composition. Gede-Salak samples are made up of a mixture of phenocrysts with different degrees of disequilibrium. Some are in equilibrium with host magma, while others may have more primary or evolved features. This observation suggests that the erupted lava is a mixture of crystals equilibrated at different depths in the plumbing system (Giacomoni *et al.*, 2016). The summary of the phenocryst assemblage is depicted in Figure 19.

The assemblage of orthopyroxene ($Mg\#_{64}$), clinopyroxene ($Mg\#_{62}$), and plagioclase ($An_{40}$) are regarded to constitute a felsic series assemblage. The plagioclase population of the lava flow and peripheral dome suggests that mafic magma contributed to the addition of medium and high An ($An_{60}$ and $An_{84}$). The addition is more prominent in younger and more evolved lava flow and peripheral dome samples. The clinopyroxene population exhibits a similar pattern. Low-Mg# pyroxene is in equilibrium with rock compositions with ${}^{Fe\text{-}Mg}KD_{min/liq}$ values of 0.24-0.31 for clinopyroxene (Sisson and Grove, 1993) and 0.23-0.35 for orthopyroxene (Putirka, 2008). Additional high-Mg pyroxene ($Mg\#_{74}$) was out of equilibrium with the composition of the rock.

Meanwhile, the assemblage of the mafic series is composed of clinopyroxene ($Mg\#_{74}$), orthopyroxene ($Mg\#_{74}$), and plagioclase ($An_{84}$). High-Mg# clinopyroxene and orthopyroxene are predominantly found as glomerocrysts and in equilibrium with each other, indicating an equivalent magma condition (${}^{Fe\text{-}Mg}KD_{aug/en} \sim 1$) (Sisson and Grove, 1993). The lava flow and peripheral dome assemblage are thought to result from a felsic series assembly that experienced several mafic magma recharges. It is substantiated that the felsic pyroxene and plagioclase textures exhibited more complex disequilibrium characteristics than their mafic counterparts. Furthermore, the high-An core exhibits considerable ascent-related pressure decrease-induced texture.

The intermediate series assemblage comprises amphibole ($Mg\#_{\sim 68}$) and plagioclase ($An_{\sim 60}$). Amphiboles are exclusively present in the summit dome and equilibrium with rock composition with ${}^{Fe\text{-}Mg}KD_{min/liq}$ value of 0.17-0.39 (Putirka, 2016). No pyroxene in the summit dome was compatible with the rock composition. Consequently, each pyroxene was derived from the mafic series. It is strengthened by the fact

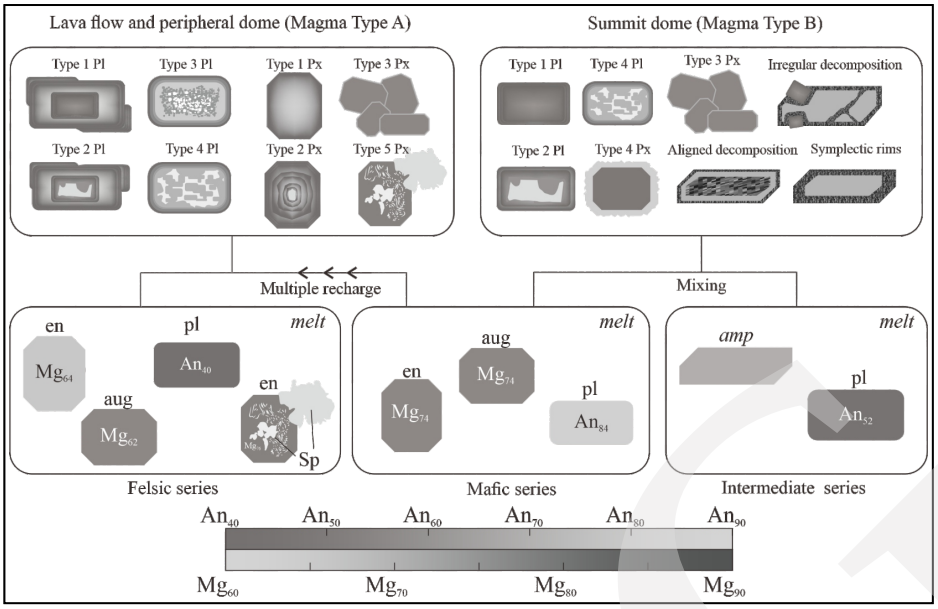


Figure 19. Origin of phenocrysts is deduced from the compositional equilibrium among series.A bar below represents the scale of anorthite content and magnesium number.

Table 4. Geothermobarometer Calculation Results for Gede-Salak Volcano (Values of temperature and pressure are given as average and range)

| Unit | | Mineral | Model | T (°C) | P (kbar) | Depth (km) |
|---|---|---|---|---|---|---|
| Lava flow | Batu lava | Clinopyroxene-melt | Putirka (2008); Neave and Putirka (2017) | 948(±13) | 4.37 (±0.50) | 16.2 |
| | | Two pyroxenes | Putirka (2008) | 1065(±77) | 5.99(±0.71) | 21.8 |
| | Salak lava | Clinopyroxene-melt | Putirka (2008); Neave and Putirka (2017) | 941(±77) | 3.93(±1.23) | 14.7 |
| | | Two pyroxenes | Putirka (2008) | 1087(±60) | 5.88(±1.67) | 21.4 |
| Peripheral dome | Wadas dome | Clinopyroxene-melt | Putirka (2008); Neave and Putirka (2017) | 933(±67) | 4.01(±0.73) | 15.0 |
| | | Two pyroxenes | Putirka (2008) | 1021(±56) | 5.39(±1.39) | 19.8 |
| Summit dome | Peda dome | Amphibole-Plagioclase | Holland and Blundy (1994) | 1010(±62) | 4.17 (±0.54) | 15.5 |
| | | Amphibole only | Ridolfi (2021) | 1011(±34) | 4.11(±0.58) | 16.4 |
| | | Two pyroxenes | Putirka (2008) | 1081(±67) | 5.77 (±1.32) | 21.1 |

that all pyroxenes in the summit dome indeed have a dusty rim, as it is ascended to different magma compositions. Compared to the lava flow and peripheral dome, the summit dome is considered the culmination of a simple mixing between the intermediate and mafic series. The plagioclase population of the summit dome suggested a proportionate amount of medium An core from the intermediate series and high An core from mafic series ($An_{60}$ and $An_{80}$). Moreover, summit dome minerals exhibit less complex disequilibrium features than lava flow and peripheral dome minerals.

**Magma Plumbing of Gede-Salak and Its Comparison among West Java Volcanoes**

Thermobarometry calculation was employed for each series previously determined. The thermobarometry calculation yielded variations in temperature and pressure, shown in Table 4. Temperature and conditions seem to correspond with the origin of crystallization phenocryst. There are basically three distinctive crystallization conditions beneath the Gede-Salak Volcano (Figure 20).

Every pair of glomerocryst clinopyroxene-orthopyroxene yielded similar temperature and

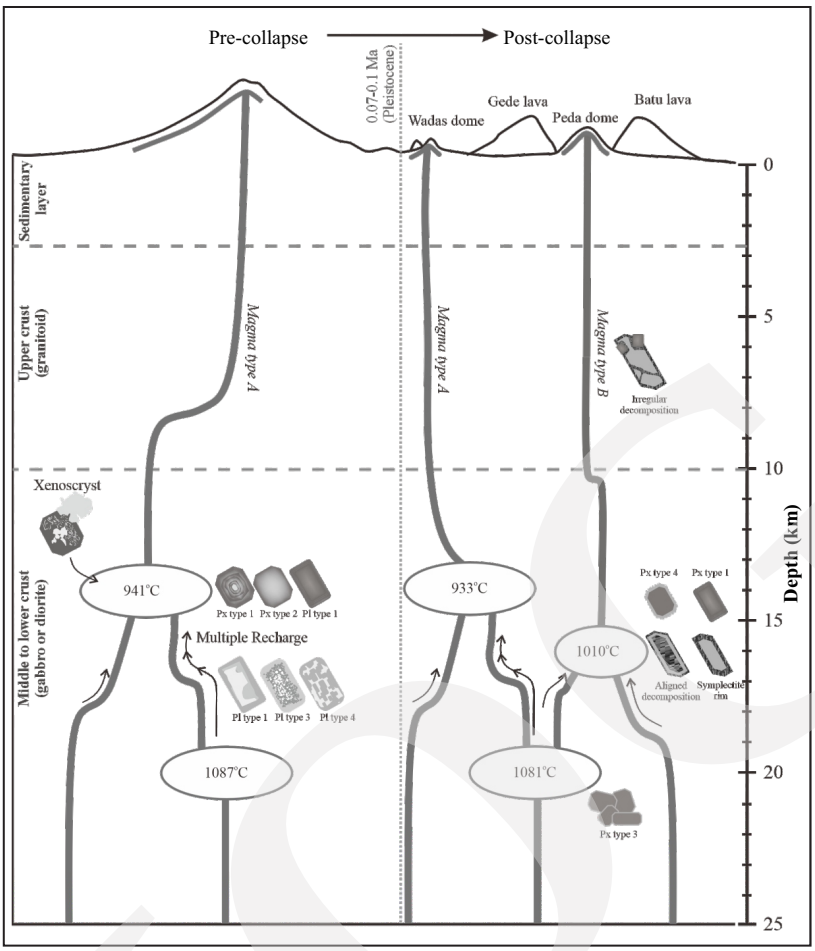


Figure 20. Schematic illustration of the magma plumbing system beneath Gede-Salak Volcano based on thermobarometry calculation. It shows that the primary magma storage is at the mid-crustal level, while only mafic magma resides in the lower-crustal level.

pressure estimates, with a range of 1065-1087°C and 5.77-5.99 kbar. The condition is considered as the origin of mafic series crystallization. Since no evolved pyroxene pair was available in the samples, the temperature and pressure of the felsic series were estimated using the clinopyroxene-melt thermobarometry. The calculation projected crystallization conditions of 933-948°C and 3.93-4.37 kbar. As no pyroxene is in equilibrium with the intermediate series rock composition, the temperature and pressure conditions were estimated using the amphibole-plagioclase pair and a single amphibole. The model predicted crystallization temperature and pressure conditions of 1010-1012°C and 4.13-4.55.

Finally, crystallization depth was calculated in order to construct magma plumbing. The calculation resulted in magma plumbing, as depicted in Figure 21. Higher crystallization temperatures correlate to greater emplacement depth. This process is recorded in phenocrysts with varying crystallization temperatures. An extensive range of temperatures is consistent with the multimodal composition of mineral and open process-induced textures. It suggests that the temperature fluctuated throughout the lengthy evolution of the magma. The magmatism of lava flows resulted from two distinguishable magmas. Throughout the course of its evolution, the felsic magma in the middle crust is periodically supplied with mafic magma from the lower crust. Following the sector collapse, magma was then emplaced as a linear arranged group of peripheral domes, which ascended through the NW-SE

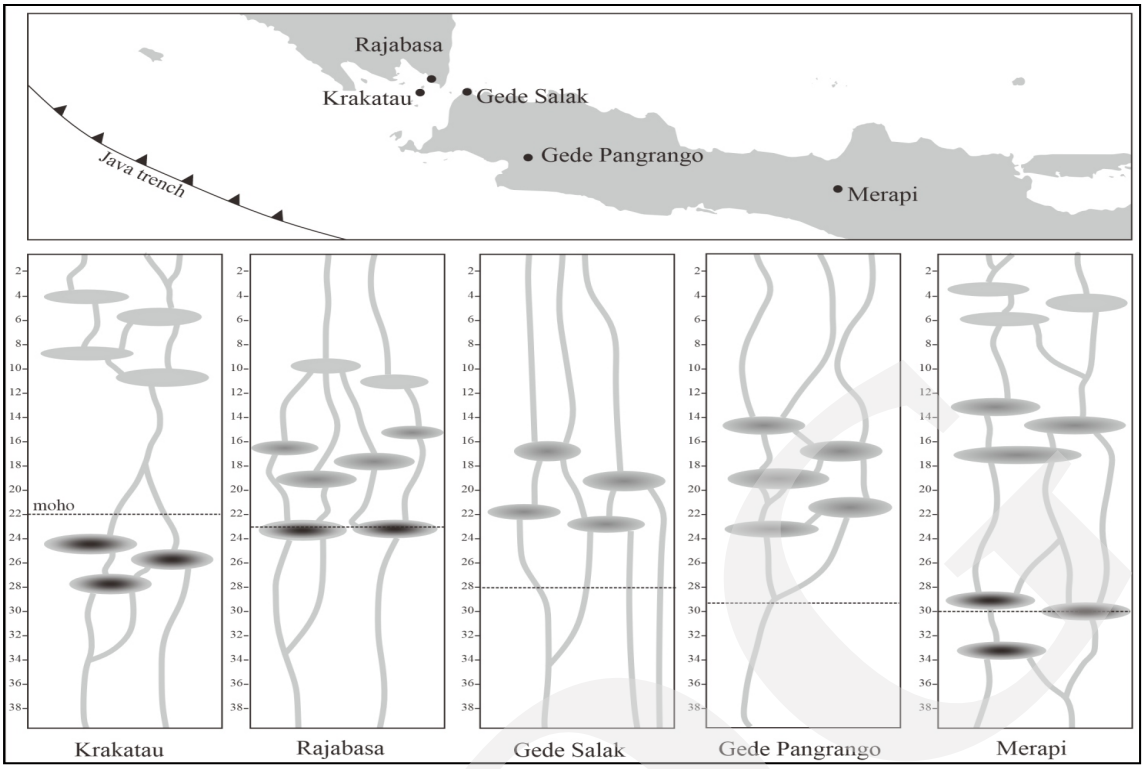


Figure 21. General model is of magma plumbing of volcanoes in West Java derived from geobarometry based on various literature.

fault system. The initial source of the summit dome was magma at the mid-crustal level. Then, at a later stage, considerably hotter and deeper mafic magma was injected into the magma and mingled with it. This process yields proportioned bimodal compositions in plagioclase and orthopyroxene phenocrysts.

Regional comparison between the primary crystallization levels of plagioclase, pyroxene, and amphibole as revealed by thermobarometry for Gede-Pangrango (two-pyroxene) (Handley *et al.*, 2010), Krakatau (plagioclase and clinopyroxene) (Dahren *et al*., 2012), Merapi (plagioclase, amphibole, clinopyroxene, and orthopyroxene) (Chadwick *et al.*, 2013; Costa *et al.*, 2013; Deegan *et al.*, 2016; Nadeau *et al.*, 2013; Preece *et al.*, 2014), Rajabasa (amphibole, clinopyroxene, and two-pyroxene) (Hasibuan, 2020), and Gede-Salak (this study) is depicted in Figure 21. The magma plumbing model of Gede-Salak Volcano is generally compatible with West Java volcanoes. Crystallization of clinopyroxene, amphibole, and high-An plagioclase occurred in lower crustal magma reservoirs (4.40 to 7.60 kbar, ~20 km depth). In several cases, pyroxene crystallization appears to also occur in the mid-crust (0.50 to 3.80 kbar, ~10 to 15 km).

Few Java suites possess significant modal amphiboles. At subduction zones, amphibole fractionation occurs at mid-crustal depths and with high water concentrations (Fischer and Marty, 2005). In Rajabasa, amphibole crystallizes at 13-15 km depth (919-928°C and 3.6-4.3 kbar). Merapi amphibole phenocryst crystallizes at depths of 8 to 15 km (900 to 950 °C and 2.5 to 4.5 MPa) and 16 to 23 km (900 to 1050 °C and 6.5-8 kbar). Gede-Salak amphibole crystallizes in ~14 - 16 km (991-1025°C and 3.8-4.2 kbar). The condition is comparable to the mid-crustal depth crystallization observed in Rajabasa and Merapi.

## Conclusions

Gede-Salak volcanism commenced with the eruption of andesitic lava flows. The subsequent

event was a ~8 km$^2$ sector collapse at the southeast flank, depositing debris avalanched. Lava domes characterized the most recent activity. Two summit domes are located in the centre of the volcano, while small peripheral lava domes are distributed on the southeast flank with NW-SE alignments.

Differences in amphibole presence and trend in K/Rb, Nb/Ta, Zr/Hf, and Sr/Y against $SiO_2$ implied two different magma types, namely type A for lava flow and peripheral dome and type B for summit dome. The trend of La/Yb and Dy/Yb against $SiO_2$ and concave REE patterns highlights the role of amphibole fractionation in magma type B. The trend of K/Rb vs. Rb demonstrates differentiation between magma types. The combination K/Rb vs. Rb trend and modal mineral core distribution suggest magma mixing.

Mineral textures indicated open system processes. Plagioclase and pyroxene phenocrysts showed chemically evolved cores with major resorption surfaces and less evolved mantles. The multiple zones of dissolution-overgrowth in the lava flow and peripheral dome suggested a repetitive change. Amphibole phenocrysts also support an open system indicated by the symplectite rim and volumetric decomposition.

The origin of the phenocrysts was determined by the assemblages of early-formed crystals established by finding the mutual chemical equilibrium. Three magma series were identified: mafic, intermediate, and felsic series. Variations in temperature and pressure estimates of thermobarometry also reveal three crystallization origins. Subsequently, felsic, intermediate, and mafic series show temperature estimates of 933-948°C, 1010-1011°C, and 1065-1087°C, consecutively. The depth calculation resulted in primary magma storage at 14 km to 17 km at the mid-crustal level. The mafic series resided in the lower crustal at 21 km.

## Acknowledgments

The authors would like to express their gratitude to the P.T. Istaka Karya staff and Mekarsari Village residents who provided valuable assistances during the field research phase. The authors would also like to thank Petrology Laboratory of Universitas Padjadjaran and Petrology and Volcanology Laboratory of Akita University for providing facilities and equipment to finish this study. The first author is a graduate student at a double degree programme of Universitas Padjadjaran and Akita University, where this work is a component of a master thesis.

## References

Anggono, T., Syuhada, S., Febriani, F., Handayani, L., Mukti, M.M., and Amran, A., 2020. Crustal shear-wave velocity structure in Western Java, Indonesia from analyses of teleseismic receiver functions. *Journal of Earth System Science,* 129, 22pp. DOI: 10.1007/s12040-019-1288-1.

Blundy, J. and Cashman, K., 2005. Rapid decompression-driven crystallization recorded by melt inclusions from Mount St. Helens volcano. *Geology,* 33 (10), p.793. DOI: 10.1130/G21668.1.

Buckley, V.J.E., Sparks, R.S.J., and Wood, B.J., 2006. Hornblende dehydration reactions during magma ascent at Soufrière Hills Volcano, Montserrat. *Contributions to Mineralogy and Petrology,* 151 (2), p.121-140. DOI: 10.1007/s00410-005-0060-5.

Burchardt, S., 2018. Introduction to Volcanic and Igneous Plumbing Systems-Developing a Discipline and Common Concepts. *In*: Burchardt, S. (ed.), *Volcanic and Igneous Plumbing Systems Elsevier*. DOI: 10.1016/B978-0-12-809749-6.00001-7.

Cashman, K. and Blundy, J., 2013. Petrological cannibalism: the chemical and textural consequences of incremental magma body growth. *Contributions to Mineralogy and Petrology,* 166 (3), p.703-729. DOI: 10.1007/s00410-013-0895-0.

Chadwick, J.P., Troll, V.R., Waight, T.E., van der Zwan, F.M., and Schwarzkopf, L.M., 2013. Pe-

trology and geochemistry of igneous inclusions in recent Merapi deposits: a window into the sub-volcanic plumbing system. *Contributions to Mineralogy and Petrology,* 165 (2), p.259-282. DOI: 10.1007/s00410-012-0808-7.

Cioni, R., Marianelli, P., and Santacroce, R., 1998. Thermal and compositional evolution of the shallow magma chambers of Vesuvius: Evidence from pyroxene phenocrysts and melt inclusions. *Journal of Geophysical Research: Solid Earth,* 103 (B8), p.18277-18294. DOI: 10.1029/98JB01124.

Coote, A.C. and Shane, P., 2016. Crystal origins and magmatic system beneath Ngauruhoe volcano (New Zealand) revealed by plagioclase textures and compositions. *Lithos,* 260, p.107-119. DOI: 10.1016/j.lithos.2016.05.017.

Costa, F., Andreastuti, S., Bouvet de Maisonneuve, C., and Pallister, J.S., 2013. Petrological insights into the storage conditions, and magmatic processes that yielded the centennial 2010 Merapi explosive eruption. *Journal of Volcanology and Geothermal Research,* 261, p.209-235. DOI: 10.1016/j.jvolgeores.2012.12.025.

Costa, F., Dohmen, R., and Chakraborty, S., 2008. Time Scales of Magmatic Processes from Modeling the Zoning Patterns of Crystals. *Reviews in Mineralogy and Geochemistry,* 69 (1), p.545-594. DOI: 10.2138/rmg.2008.69.14.

Dahren, B., Troll, V.R., Andersson, U.B., Chadwick, J.P., Gardner, M.F., Jaxybulatov, K., and Koulakov, I., 2012. Magma plumbing beneath Anak Krakatau Volcano, Indonesia: evidence for multiple magma storage regions. *Contributions to Mineralogy and Petrology,* 163 (4), p.631-651. DOI: 10.1007/s00410-011-0690-8.

Davidson, J., Turner, S., Handley, H., Macpherson, C., and Dosseto, A., 2007. Amphibole "sponge" in arc crust? *Geology,* 35 (9), p.787. DOI: 10.1130/G23637A.1.

De Angelis, S.H., Larsen, J., and Coombs, M., 2013. Pre-eruptive Magmatic Conditions at Augustine Volcano, Alaska, 2006: Evidence from Amphibole Geochemistry and Textures. *Journal of Petrology,* 54 (9), p.1939-1961. DOI: 10.1093/petrology/egt037.

De Angelis, S.H., Larsen, J., Coombs, M., Dunn, A., and Hayden, L., 2015. Amphibole reaction rims as a record of pre-eruptive magmatic heating: An experimental approach. *Earth and Planetary Science Letters,* 426, p.235-245. DOI: 10.1016/j.epsl.2015.06.051.

Deegan, F.M., Whitehouse, M.J., Troll, V.R., Budd, D.A., Harris, C., Geiger, H., and Hålenius, U., 2016. Pyroxene standards for SIMS oxygen isotope analyses and their application to Merapi volcano, Sunda arc, Indonesia. *Chemical Geology,* 447, p.1-10. DOI: 10.1016/j.chemgeo.2016.10.018.

De Silva, S. and Lindsay, J.M., 2015. Primary Volcanic Landforms. *In*: H. Sigurdsson (ed.), *The Encyclopedia of Volcanoes*. Elsevier, p.273-297. DOI: 10.1016/B978-0-12-385938-9.00015-8.

Dessimoz, M., Müntener, O., and Ulmer, P., 2012. A case for hornblende dominated fractionation of arc magmas: the Chelan Complex (Washington Cascades). *Contributions to Mineralogy and Petrology*, 163 (4), p.567-589. DOI: 10.1007/s00410-011-0685-5.

D'Mello, N.G., Zellmer, G.F., Negrini, M., Kereszturi, G., Procter, J., Stewart, R., Prior, D., Usuki, M., and Iizuka, Y., 2021. Deciphering magma storage and ascent processes of Taranaki, New Zealand, from the complexity of amphibole breakdown textures. *Lithos*, 398-399, p.106264. DOI: 10.1016/j.lithos.2021.106264.

Efimov, A.A. and Malitch, K.N., 2012. Magnetite-orthopyroxene symplectites in gabbros of the Urals: A structural track of olivine oxidation. *Geology of Ore Deposits,* 54 (7), p.531-539. DOI: 10.1134/S1075701511070075.

Fischer, T.P. and Marty, B., 2005. Volatile abundances in the sub-arc mantle: insights from volcanic and hydrothermal gas discharges. *Journal of Volcanology and Geothermal Research,* 140 (1-3), p.205-216. DOI: 10.1016/j.jvolgeores.2004.07.022.

Giacomoni, P.P., Coltorti, M., Bryce, J.G., Fahnestock, M.F., and Guitreau, M., 2016. Mt. Etna plumbing system revealed by combined tex-

tural, compositional, and thermobarometric studies in clinopyroxenes. *Contributions to Mineralogy and Petrology,* 171 (4), 15pp. DOI: 10.1007/s00410-016-1247-7.

Gill, J.B., 1981. *Orogenic Andesites and Plate Tectonics*. Springer, Berlin. DOI: 10.1007/978-3-642-68012-0

Ginibre, C., Kronz, A., and Wörner, G., 2002. High-resolution quantitative imaging of plagioclase composition using accumulated backscattered electron images: new constraints on oscillatory zoning. *Contributions to Mineralogy and Petrology,* 142 (4), p.436-448. DOI: 10.1007/s004100100298.

Green, N. and Powell, J., 2006. Amphibole-controlled Differentiation of High-Mg Andesite Magmas in a Hot Subduction Environment. *Proceedings, AGU Fall Meeting*, San Francisco.

Habtoor, A.M., Ahmed, A.H., Al-Akhaly, I.A., Harbi, H.M., and Said, N.M., 2022. Orthopyroxene-magnetite symplectites in gabbro of Gabal Taftafan, western Arabian Shield, Saudi Arabia. *Arabian Journal of Geosciences,* 15 (6), p.524. DOI: 10.1007/s12517-022-09812-x.

Hall, R., 2012. Late Jurassic-Cenozoic reconstructions of the Indonesian region and the Indian Ocean. *Tectonophysics,* 570-571, p.1-41. DOI: 10.1016/j.tecto.2012.04.021.

Hamilton, W., 1973. Tectonics of the Indonesian Region. *Bulletin of the Geological Society of Malaysia,* 6, p.3-10. DOI: 10.7186/bgsm06197301.

Hammer, J.E. and Rutherford, M.J., 2002. An experimental study of the kinetics of decompression-induced crystallization in silicic melt. *Journal of Geophysical Research: Solid Earth,* 107 (B1), p.ECV 8-1-ECV 8-24. DOI: 10.1029/2001JB000281.

Handley, H.K., Blichert-Toft, J., Gertisser, R., Macpherson, C.G., Turner, S.P., Zaennudin, A., and Abdurrachman, M., 2014. Insights from Pb and O isotopes into along-arc variations in subduction inputs and crustal assimilation for volcanic rocks in Java, Sunda arc, Indonesia. *Geochimica et Cosmochimica Acta,* 139, p.205-226. DOI: 10.1016/j.gca.2014.04.025.

Handley, H.K., Davidson, J.P., Macpherson, C.G., and Stimac, J.A., 2008. Untangling differentiation in arc lavas: Constraints from unusual minor and trace element variations at Salak Volcano, Indonesia. *Chemical Geology,* 255 (3-4), p.360-376. DOI: 10.1016/j.chemgeo.2008.07.007.

Handley, H.K., Macpherson, C.G., and Davidson, J.P., 2010. Geochemical and Sr-O isotopic constraints on magmatic differentiation at Gede Volcanic Complex, West Java, Indonesia. *Contributions to Mineralogy and Petrology,* 159 (6), p.885-908. DOI: 10.1007/s00410-009-0460-z.

Handley, H.K., Macpherson, C.G., Davidson, J.P., Berlo, K., and Lowry, D., 2007. Constraining Fluid and Sediment Contributions to Subduction-Related Magmatism in Indonesia: Ijen Volcanic Complex. *Journal of Petrology,* 48 (6), p.1155-1183. DOI: 10.1093/petrology/egm013.

Harjono, H., Diament, M., Dubois, J., Larue, M., and Zen, M.T., 1991. Seismicity of the Sunda Strait: Evidence for crustal extension and volcanological implications. *Tectonics,* 10 (1), p.17-30. DOI: 10.1029/90TC00285.

Hasibuan, R.F., 2020. T*he evolution of magma plumbing system in Tangkil and Rajabasa volcanoes, Indonesia. PhD Thesis* at Department of Geoscience, Geotechnology, and Material Resource Engineering, Akita University

Hawthorne, F.C., Oberti, R., Harlow, G.E., Maresch, W.V., Martin, R F., Schumacher, J.C., and Welch, M.D., 2012. Nomenclature of the amphibole supergroup. *American Mineralogist,* 97 (11-12), p.2031-2048. DOI: 10.2138/am.2012.4276.

Hayes, G.P., Moore, G.L., Portner, D.E., Hearne, M., Flamme, H., Furtney, M., and Smoczyk, G.M., 2018. Slab2, a comprehensive subduction zone geometry model. *Science,* 362 (6410), p.58-61. DOI: 10.1126/science.aat4723.

Hildreth, W. and Moorbath, S., 1988. Crustal contributions to arc magmatism in the Andes

of Central Chile. *Contributions to Mineralogy and Petrology,* 98 (4), p.455-489. DOI: 10.1007/BF00372365.

Holland, T. and Blundy, J., 1994. Non-ideal interactions in calcic amphiboles and their bearing on amphibole-plagioclase thermometry. *Contributions to Mineralogy and Petrology,* 116 (4), p.433-447. DOI: 10.1007/BF00310910.

Huchon, P. and Le Pichon, X., 1984. Sunda Strait and Central Sumatra fault. *Geology,* 12 (11), 668. DOI: 10.1130/0091-7613(1984)12<668:SSACSF>2.0.CO;2.

Irvine, T.N. and Baragar, W.R.A., 1971. A Guide to the Chemical Classification of the Common Volcanic Rocks. *Canadian Journal of Earth Sciences,* 8 (5), p.523-548. DOI: 10.1139/e71-055.

Jakeš, P. and White, A.J.R., 1970. ratios of rocks from island arcs. *Geochimica et Cosmochimica Acta,* 34 (8), p.849-856. DOI: 10.1016/0016-7037(70)90123-7.

Kimura, J.I., Gill, J.B., Kunikiyo, T., Osaka, I., Shimoshioiri, Y., Katakuse, M., Kakubuchi, S., Nagao, T., Furuyama, K., Kamei, A., Kawabata, H., Nakajima, J., Van Keken, P.E., and Stern, R.J., 2014. Diverse magmatic effects of subducting a hot slab in SW Japan: Results from forward modeling. *Geochemistry, Geophysics, Geosystems,* 15 (3), p.691-739. DOI: 10.1002/2013GC005132.

Kopp, H., Flueh, E.R., Klaeschen, D., Bialas, J., and Reichert, C., 2001. Crustal structure of the central Sunda margin at the onset of oblique subduction. *Geophysical Journal International,* 147 (2), p.449-474. DOI: 10.1046/j.0956-540x.2001.01547.x.

Kurniawan, I.A., Suparka, E., Abdurrachman, M., and Hasenaka, T., 2013. Petrology and Geochemistry of Gede-Salak Volcano Northwest Java: Evolution of magmatic process. *Proceeding, IAVCEI*, Kagoshima.

Kurniawan, I.A., Suparka, E., Hasenaka, T., and Suparka, E., 2011. Quatenary Gede-Salak volcanic complex, Banten area, at the junction between Sumatra arc and Java arc, Indonesia. *Japan Geoscience Union Meeting*, Chiba.

Le Bas, M.J.L., Maitre, R.W.L., Streckeisen, A., Zanettin, B., and Zanetin, B., 1986. A Chemical Classification of Volcanic Rocks Based on the Total Alkali-Silica Diagram. *Journal of Petrology,* 27 (3), p.745-750. DOI: 10.1093/petrology/27.3.745.

Li, L., Xiong, X.L., and Liu, X.C., 2017. Nb/Ta fractionation by amphibole in hydrous basaltic systems: Implications for arc magma evolution and continental crust formation. *Journal of Petrology,* 58 (1), p.3-28. DOI: 10.1093/petrology/egw070.

Linnen, R.L. and Keppler, H., 2002. Melt composition control of Zr/Hf fractionation in magmatic processes. *Geochimica et Cosmochimica Acta,* 66 (18), p.3293-3301. DOI: 10.1016/S0016-7037(02)00924-9.

McDonough, W.F. and Sun, S., 1995. The composition of the Earth. *Chemical Geology,* 120 (3-4), p.223-253. DOI: 10.1016/0009-2541(94)00140-4.

Miyashiro, A., 1974. Volcanic rock series in island arcs and active continental margins. *American Journal of Science,* 274 (4), p.321-355. DOI: 10.2475/ajs.274.4.321.

Nadeau, O., Williams-Jones, A.E., and Stix, J., 2013. Magmatic-hydrothermal evolution and devolatilization beneath Merapi volcano, Indonesia. *Journal of Volcanology and Geothermal Research,* 261, p.50-68. DOI: 10.1016/j.jvolgeores.2013.04.006.

Nandedkar, R.H., Hürlimann, N., Ulmer, P., and Müntener, O., 2016. Amphibole-melt trace element partitioning of fractionating calc-alkaline magmas in the lower crust: an experimental study. *Contributions to Mineralogy and Petrology,* 171 (8-9), 71p. DOI: 10.1007/s00410-016-1278-0.

Neave, D.A. and Putirka, K.D., 2017. A new clinopyroxene-liquid barometer, and implications for magma storage pressures under Icelandic rift zones. *American Mineralogist,* 102 (4), p.777-794. DOI: 10.2138/am-2017-5968.

Ohba, T., Kimura, Y., and Fujimaki, H. 2007. High-Magnesian Andesite Produced by Two-Stage Magma Mixing: a Case Study

from Hachimantai, Northern Honshu, Japan. *Journal of Petrology,* 48 (3), 627-645. DOI: 10.1093/petrology/egl075.

Pearce, T.H., 1994. Recent Work on Oscillatory Zoning in Plagioclase. *In*: Parson I. (ed.), *Feldspars and their Reactions*. Springer, p.313-349. DOI: 10.1007/978-94-011-1106-5_8.

Plechov, P.Y., Tsai, A.E., Shcherbakov, V.D., and Dirksen, O.V., 2008. Opacitization conditions of hornblende in Bezymyannyi volcano andesites (March 30, 1956 eruption). *Petrology,* 16 (1), p.19-35. DOI: 10.1134/S0869591108010025.

Pramumijoyo, S. and Sebrier, M., 1991. Neogene and quaternary fault kinematics around the Sunda Strait area, Indonesia. *Journal of Southeast Asian Earth Sciences,* 6 (2), p.137-145. DOI: 10.1016/0743-9547(91)90106-8.

Preece, K., Gertisser, R., Barclay, J., Berlo, K., and Herd, R.A., 2014. Pre- and syn-eruptive degassing and crystallisation processes of the 2010 and 2006 eruptions of Merapi volcano, Indonesia. *Contributions to Mineralogy and Petrology,* 168 (4), 1061pp. DOI: 10.1007/s00410-014-1061-z.

Putirka, K.D. 2008. Thermometers and Barometers for Volcanic Systems. *Reviews in Mineralogy and Geochemistry,* 69 (1), p.61-120. DOI: 10.2138/rmg.2008.69.3.

Putirka, K.D., 2016. Amphibole thermometers and barometers for igneous systems and some implications for eruption mechanisms of felsic magmas at arc volcanoes. *American Mineralogist,* 101 (4), p.841-858. DOI: 10.2138/am-2016-5506.

Ridolfi, F., 2021. Amp-TB2: An Updated Model for Calcic Amphibole Thermobarometry. *Minerals,* 11 (3), p.324. DOI: 10.3390/min11030324.

Ruprecht, P. and Wörner, G., 2007. Variable regimes in magma systems documented in plagioclase zoning patterns: El Misti stratovolcano and Andahua monogenetic cones. *Journal of Volcanology and Geothermal Research,* 165 (3-4), p.142-162. DOI: 10.1016/j.jvolgeores.2007.06.002.

Rusmana, E., Suwitodirjo, K., and Suharsono., 1991. *Geological Map of Serang Quadrangle, Jawa. scale 1:250.000*. Geological Research and Development Centre, Bandung.

Sendjaja, Y.A., Kimura, J.I., and Sunardi, E., 2009. Across-arc geochemical variation of Quaternary lavas in West Java, Indonesia: Mass-balance elucidation using arc basalt simulator model. *Island Arc,* 18 (1), p.201-224. DOI: 10.1111/j.1440-1738.2008.00641.x.

Shibata, T., Yoshimoto, M., Fujii, T., and Nakada, S., 2015. Geochemical and Sr-Nd isotopic characteristics of Quaternary Magmas from the Pre-Komitake volcano. *Journal of Mineralogical and Petrological Sciences,* 110 (2), p.65-70. DOI: 10.2465/jmps.141022e.

Sisson, T.W. and Grove, T.L., 1993. Experimental investigations of the role of $H_2O$ in calc-alkaline differentiation and subduction zone magmatism. *Contributions to Mineralogy and Petrology,* 113 (2), p.143-166. DOI: 10.1007/BF00283225.

Streck, M.J., 2008. Mineral Textures and Zoning as Evidence for Open System Processes. *Reviews in Mineralogy and Geochemistry,* 69 (1), p.595-622. DOI: 10.2138/rmg.2008.69.15.

Streck, M.J., Broderick, C.A., Thornber, C.R., Clynne, M.A., and Pallister, J.S., 2008. Plagioclase populations and zoning in dacite of the 2004-2005 Mount St. Helens eruption: Constraints for magma origin and dynamics. *In*: Sherrod, D.R., Scott, W.E., and Stauffer, P.H. (eds.), *A Volcano Rekindled: The Renewed Eruption of Mount St. Helens, 2004-2006*, U.S. Geological Survey Professional Paper 1750, p.791-808. DOI: 10.3133/pp175034.

Streck, M.J., Leeman, W.P., and Chesley, J., 2007. High-magnesian andesite from Mount Shasta: A product of magma mixing and contamination, not a primitive mantle melt. *Geology,* 35 (4), p.351. DOI: 10.1130/G23286A.1.

Sun, S. and McDonough, W.F., 1989. Chemical and isotopic systematics of oceanic basalts: implications for mantle composition and processes. *Geological Society, London, Spe-*

*cial Publications,* 42 (1), p.313-345. DOI: 10.1144/GSL.SP.1989.042.01.19.

Suntoko, H. and Mellawati, J., 2014. Studi Kelurusan Sesar Banten-1 di Calon Tapak. *Proceedings, Seminar Nasional Geologi Nuklir Dan Sumber Daya Tambang Tahun 2014*, Jakarta.

Suntoko, H. and Nugroho, A., 2011. Analisis Gradient Horizontal (Graviti) untuk Konfimasi Awal Sesar Permukaan di Tapak Banten. *Jurnal Pengembangan Energi Nuklir,* 13 (2), p.72-80.

Suntoko, H., Nurdin, M., Susilo, Y.S.B., and Hamzah, I., 2012. Pendeteksian Keberadaan Struktur Sesar pada Batuan Vulkanik dengan Metode Magnetik. *EKSPLORIUM,* 33 (2), p.111-120. DOI: 10.17146/eksplorium.2012.33.2.2661.

Viccaro, M., Giacomoni, P.P., Ferlito, C., and Cristofolini, R., 2010. Dynamics of magma supply at Mt. Etna volcano (Southern Italy) as revealed by textural and compositional features of plagioclase phenocrysts. *Lithos,* 116 (1-2), p.77-91. DOI: 10.1016/j.lithos.2009.12.012.

Wibowo, H.E., 2017. P*etrological and Geochemical Study of Sundoro Volcano, Central Java, Indonesia : Temporal Variation in Differentiation and Source Processes in the Growth of an Individual Volcano. PhD. Thesis* at Department of Natural History Sciences, Hokkaido University. DOI: 10.14943/doctoral.k12699.

Wibowo, H.E., Nakagawa, M., Kuritani, T., Furukawa, R., Prambada, O., and Harijoko, A., 2022. Petrological and Geochemical Study of Sundoro Volcano, Central Java, Indonesia: Temporal Variations in Differentiation and Source Processes During the Growth of an Individual Volcano. *Journal of Petrology,* 63 (9), p.1-22. DOI: 10.1093/petrology/egac083.

Widagdo, A., Setijadi, R., Waluyo, G., and Purwasatriya, E.B., 2021. Kehadiran Patahan Geologi di Daerah Bojanegara, Kabupaten Serang, Provinsi Banten. *GEOSAPTA,* 7 (2), p.79. DOI: 10.20527/jg.v7i2.9439.

Widiyantoro, S. and van der Hilst, R., 1997. Mantle structure beneath Indonesia inferred from high-resolution tomographic imaging. *Geophysical Journal International,* 130 (1), p.167-182. DOI: 10.1111/j.1365-246X.1997.tb00996.x.